



**HAL**  
open science

## The XUV environments of exoplanets from Jupiter-size to super-Earth

George W. King, Peter J. Wheatley, Michael Salz, Vincent Bourrier, Stefan Czesla, David Ehrenreich, James Kirk, Alain Lecavelier Des Etangs, Tom Louden, Jürgen Schmitt, et al.

► **To cite this version:**

George W. King, Peter J. Wheatley, Michael Salz, Vincent Bourrier, Stefan Czesla, et al.. The XUV environments of exoplanets from Jupiter-size to super-Earth. Monthly Notices of the Royal Astronomical Society, 2018, 478, pp.1193-1208. 10.1093/mnras/sty1110 . insu-03747690

**HAL Id: insu-03747690**

**<https://insu.hal.science/insu-03747690>**

Submitted on 8 Aug 2022

**HAL** is a multi-disciplinary open access archive for the deposit and dissemination of scientific research documents, whether they are published or not. The documents may come from teaching and research institutions in France or abroad, or from public or private research centers.

L'archive ouverte pluridisciplinaire **HAL**, est destinée au dépôt et à la diffusion de documents scientifiques de niveau recherche, publiés ou non, émanant des établissements d'enseignement et de recherche français ou étrangers, des laboratoires publics ou privés.

# The XUV environments of exoplanets from Jupiter-size to super-Earth

George W. King,<sup>1,2★</sup> Peter J. Wheatley,<sup>1,2</sup> Michael Salz,<sup>3</sup> Vincent Bourrier,<sup>4</sup>  
Stefan Czesla,<sup>3</sup> David Ehrenreich,<sup>4</sup> James Kirk,<sup>1</sup> Alain Lecavelier des Etangs,<sup>5</sup>  
Tom Loudon,<sup>1,2</sup> Jürgen Schmitt<sup>3</sup> and P. Christian Schneider<sup>3</sup>

<sup>1</sup>Department of Physics, University of Warwick, Gibbet Hill Road, Coventry CV4 7AL, UK

<sup>2</sup>Centre for Exoplanets and Habitability, University of Warwick, Gibbet Hill Road, Coventry CV4 7AL, UK

<sup>3</sup>Hamburger Sternwarte, Universität Hamburg, Gojenbergsweg 112, D-21029 Hamburg, Germany

<sup>4</sup>Observatoire de l'Université de Genève, 51 chemin des Maillettes, CH-1290 Sauverny, Switzerland

<sup>5</sup>Institut d'Astrophysique de Paris, UMR7095 CNRS, Université Pierre & Marie Curie, 98bis boulevard Arago, F-75014 Paris, France

Accepted 2018 April 27. Received 2018 April 25; in original form 2017 December 5

## ABSTRACT

Planets that reside close-in to their host star are subject to intense high-energy irradiation. Extreme-ultraviolet (EUV) and X-ray radiation (together, XUV) is thought to drive mass-loss from planets with volatile envelopes. We present *XMM-Newton* observations of six nearby stars hosting transiting planets in tight orbits (with orbital period,  $P_{\text{orb}} < 10$  d), wherein we characterize the XUV emission from the stars and subsequent irradiation levels at the planets. In order to reconstruct the unobservable EUV emission, we derive a new set of relations from Solar *TIMED/SEE* data that are applicable to the standard bands of the current generation of X-ray instruments. From our sample, WASP-80b and HD 149026b experience the highest irradiation level, but HAT-P-11b is probably the best candidate for Ly  $\alpha$  evaporation investigations because of the system's proximity to the Solar system. The four smallest planets have likely lost a greater percentage of their mass over their lives than their larger counterparts. We also detect the transit of WASP-80b in the near-ultraviolet with the optical monitor on *XMM-Newton*.

**Key words:** planets and satellites: atmospheres – stars: individual: GJ 436, GJ 3470, HAT-P-11, HD 97658, HD 149026, WASP-80 – ultraviolet: stars – X-rays: stars.

## 1 INTRODUCTION

A substantial number of the exoplanets discovered to date have orbital periods of less than 10 d, lying much closer to their host star than Mercury does to the Sun. Such close-in planets are subject to strong irradiation by their parent star. High-energy photons at extreme-ultraviolet (EUV) and X-ray wavelengths are thought to drive hydrodynamic winds from planetary atmospheres. It has been suggested that super-Earth and Neptune-sized planets may be susceptible to losing a significant portion of their mass through this process (e.g. Owen & Jackson 2012; Lopez & Fortney 2013). In the most extreme cases, complete atmospheric evaporation and evolution to a largely rocky planet may be possible. This is an area of particular interest given past studies that point to a dearth of hot Neptunes at the very shortest periods, where high-energy irradiation is at its greatest (e.g. Lecavelier Des Etangs 2007; Davis & Wheatley 2009; Ehrenreich & Désert 2011; Szabó & Kiss 2011; Beaugé & Nesvorný 2013; Helled, Lozovsky & Zucker 2016). This shortage

cannot be explained by selection effects. In contrast, hot Jupiters should lose only a few per cent of their envelope on time-scales of the order of Gyr (e.g. Murray-Clay, Chiang & Murray 2009; Owen & Jackson 2012).

Detections of substantial atmospheric expansion and mass-loss have been inferred in a few cases as significant increases in the observed transit depth in ultraviolet lines, particularly around the Ly  $\alpha$  line which probes neutral hydrogen. The first such inference was made by Vidal-Madjar et al. (2003), who detected in-transit absorption in the Ly  $\alpha$  line 10 times that expected from the optical transit of HD 209458b. This depth pointed to absorption from a region larger than the planet's Roche lobe, leading to the conclusion of an evaporating atmosphere. The light curve also showed an early ingress and late egress. Ly  $\alpha$  observations of HD 189733b also revealed an expanded atmosphere of escaping material (Lecavelier Des Etangs et al. 2010; Lecavelier des Etangs et al. 2012; Bourrier et al. 2013). The measured Ly  $\alpha$  transit depth was measured at twice the optical depth in 2007, and six times the optical depth in 2011. The temporal variations in the transit absorption depth of the Ly  $\alpha$  line may be related to an X-ray flare detected in contemporaneous *Swift* observations in 2011. Similar signatures are beginning to be detected for

\* E-mail: g.king.5@warwick.ac.uk

sub Jovian-sized planets too. Ehrenreich et al. (2015) discovered an exceptionally deep Ly  $\alpha$  transit for GJ 436b, implying that over half of the stellar disc was being eclipsed. This is compared to the 0.69 per cent transit seen in the optical. The Ly  $\alpha$  transits show early ingress, and late egress up to 20 h after the planet's transit (Lavie et al. 2017). Recent investigations by Bourrier et al. (2017b) for the super-Earth HD 97658b suggested that it does not have an extended, evaporating hydrogen atmosphere, in contrast to predictions of observable escaping hydrogen due to the dissociation of steam. Possible explanations include a relatively low XUV irradiation, or a high-weight atmosphere. A similar non-detection for 55 Cnc e had previously been found by Ehrenreich et al. (2012). In that case, complete loss of the atmosphere down to a rocky core has not been ruled out. Most recently, a study of Kepler-444 showed strong variations in the Ly  $\alpha$  line that could arise from hydrodynamic escape of the atmosphere (Bourrier et al. 2017a), while Ly  $\alpha$  emission has been detected for TRAPPIST-1 (Bourrier et al. 2017c) and the search for evaporation signatures is ongoing.

Evidence for hydrodynamic escape also extends to lines of other elements. Deep carbon, oxygen, and silicon features have been detected for HD 209458b, and interpreted as originating in the extended atmosphere surrounding the planet (Vidal-Madjar et al. 2004; Linsky et al. 2010), the species having been entrained in the hydrodynamic flow. The Si III detection in this case has since been found to be likely due to stellar variability (Ballester & Ben-Jaffel 2015). A similar O I detection has been made for HD 189733b (Ben-Jaffel & Ballester 2013).

EUV photons are thought to be an important driving force behind atmospheric evaporation (e.g. Owen & Jackson 2012), however they are readily absorbed by the interstellar medium, making direct observations possible only for the closest and brightest stars. Additionally, since the end of the EUVE mission (Bowyer & Malina 1991) in 2001, no instrument covers this spectral range, so the EUV emission of host stars can only be derived from estimates. Lecavelier Des Etangs (2007) and Ehrenreich & Désert (2011) applied a method of reconstruction from a star's rotational velocity, using a relationship from the work of Wood et al. (1994), and several studies have looked at linking EUV output to observable wavelengths. Sanz-Forcada et al. (2011) derived an expression relating the EUV and X-ray luminosities, based on synthetic coronal models for a sample of main-sequence stars. Chadney et al. (2015) analysed solar data from the *TIMED/SEE* mission (Woods et al. 2005), determining an empirical power-law relation between the ratio of EUV to X-ray flux, and the X-ray flux at the stellar surface. Their fig. 2 suggests that this relation appears consistent with measurements of a small sample of nearby stars. Linsky, Fontenla & France (2014) approached the problem from the other direction, reconstructing the EUV emission from Ly  $\alpha$ . They combined Ly  $\alpha$  observations with EUVE measurements in the range 100–400 Å, and solar models from Fontenla et al. (2014) across 400–912 Å. This method has since been employed by the MUSCLES Treasury Survey, which has catalogued spectral energy distributions (SEDs) for 11 late-type planet hosts from X-ray through to mid-infrared (Loyd et al. 2016; Youngblood et al. 2016). An alternative approach is to perform a Differential Emission Measure recovery, as Loudon, Wheatley & Briggs (2017) did for HD 209458. This study incorporated information from both the *Hubble Space Telescope* and *XMM-Newton* on the UV line and X-ray fluxes, respectively.

Following on from Salz et al. (2015)'s investigations into hot Jupiters, we probe the high-energy environments of planets ranging from Jupiter-size down to super-Earth. All six planets in our sample orbit their parent star with a period of <10 d. Our sample is intro-

duced in Section 2. The observations are described in Section 3. Results of the X-ray analysis, as well as reconstruction of the full XUV flux, are presented in Section 4. The optical monitor (OM) results are detailed in Section 5. The implications of our analysis are discussed in Section 6. The work is summarized in Section 7.

## 2 SAMPLE

Our sample of six systems is made up of six of the closest known transiting planets to the Earth, and is listed in Table 1. Fig. 1 shows all known transiting planets within 100 pc, and highlights the objects in this sample. Each of the planets occupies a scarcely populated area of this parameter space. Together with the results of past observations with *XMM-Newton* and *ROSAT* for some of the sample, their proximity means that all of the hosts were predicted to exhibit sufficient X-ray flux for characterization of the planet's XUV irradiation.

Table 1 outlines the properties of each planetary system investigated. We note that the values for HD 149026 from Southworth (2010) differ substantially from those of Carter et al. (2009), and that this also affects our mass-loss analysis in Section 6.3.

GJ 436b, GJ 3470b, and HAT-P-11b are the three closest transiting Neptune-sized planets. Only two other transiting planets within 100 pc, K2-25b and HD 3167c, have a radius between 3 and 5  $R_{\oplus}$ , and the latter is likely to be comparatively far less irradiated than our sample. HD 149026 is the only known exoplanet within 100 pc with its radius between that of Neptune and Saturn. HD 97658b is the second closest, and orbits by far the brightest star ( $V = 7.7$  mag) of any known planet of its size. Though its importance is less obvious from Fig. 1, WASP-80 represents one of only a handful of transiting hot Jupiters in orbit around a late K/early M-type star.

In addition to the favourable X-ray characterization potential, four of the systems (GJ 436, HAT-P-11, HD 97658, and WASP-80) were also chosen in order to explore their near-ultraviolet (NUV) transit properties with the OM on *XMM-Newton*.

## 3 OBSERVATIONS

The six planet hosts were all observed by the European Photon Imaging Camera (EPIC) on *XMM-Newton* in 2015. Table 2 provides details of the observations in time, duration, and orbital phase, as well as the adopted ephemerides. Observations were taken with the OM concurrently, cycling through different filters for GJ 3470 and HD 149026. For the other four objects, a single filter was used in fast mode in an attempt to detect transits in the ultraviolet.

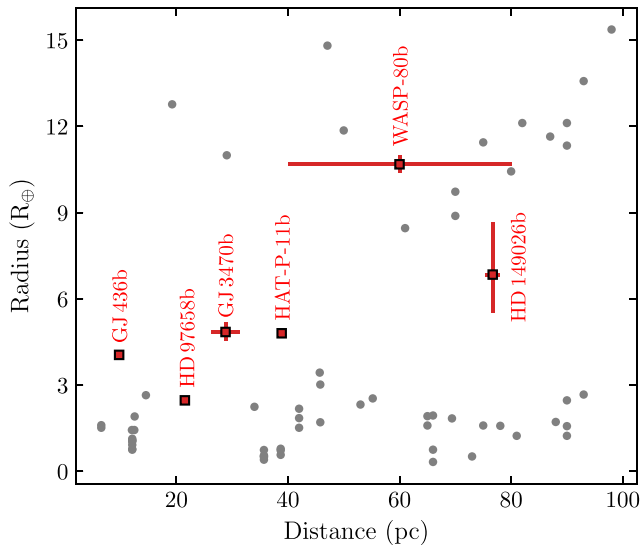
The data were reduced using the Scientific Analysis System (sas 15.0.0) following the standard procedure.<sup>1</sup> The EPIC-pn data of all systems except HD 97658 show elevated high-energy background levels at some points in the observations. To minimize loss of exposure time, we raised the default count rate threshold for time filtering due to high-energy events (>10 keV) by a factor of 2 compared to the standard value. Background filtering does not affect the results, except for HAT-P-11. High background (exceeding this higher threshold) was observed at numerous epochs in the HAT-P-11 data, as often seen in *XMM-Newton* due to Solar soft protons (Walsh et al. 2014). Although the size of the uncertainties was not significantly changed by filtering, a 10 per cent increase in the best-fitting

<sup>1</sup> As outlined on the 'SAS Threads' webpages: <http://www.cosmos.esa.int/web/xmm-Newton/sas-threads>.

**Table 1.** System parameters for the six transiting exoplanet host stars we observed with *XMM-Newton*.

System	Spectral Type	$V$ (mag)	$d$ (pc)	Age (Gyr)	$R_*$ ( $R_\odot$ )	$T_{\text{eff},*}$ (K)	$P_{\text{rot}}$ (d)	$R_p$ ( $R_J$ )	$M_p$ ( $M_J$ )	$\log g$ ( $\text{cm s}^{-2}$ )	$P_{\text{orb}}$ (d)	$a$ (au)	$e$	$T_{\text{eff},p}$ (K)
GJ 436	M2.5V	10.6	9.749	6	0.437	3585	44.09	0.361	0.0737	3.15	2.644	0.0287	0.153	740
GJ 3470	M1.5V	12.3	28.82	1–4	0.568	3600	20.7	0.432	0.0437	2.76	3.337	0.0369	0	620
HAT-P-11	K4V	9.5	37.88	5.2	0.752	4780	29.33	0.428	0.081	3.05	4.888	0.0513	0.2646	880
HD 97658	K1V	7.7	21.53	9.7	0.741	5170	38.5	0.220	0.0238	3.17	9.489	0.080	0.078	760
HD 149026	G0IV	8.1	76.7	1.2	1.290	6147	11.5	0.610	0.356	3.37	2.876	0.0429	0	1600
WASP-80	K7-M0V	11.9	60	0.1	0.571	4145	8.5	0.952	0.554	3.18	3.068	0.0346	<0.07	800

References: GJ 436: All parameters from Knutson et al. (2011) except  $d$  (*Gaia*: Gaia Collaboration et al. 2016), age and  $T_{\text{eff},*}$  (Torres 2007),  $P_{\text{rot}}$  (Bourrier et al. 2018), and  $M_p$  (Southworth 2010). GJ 3470: All from Awiphan et al. (2016), except  $d$  and  $P_{\text{rot}}$  (Biddle et al. 2014). HAT-P-11:  $R_*$ ,  $M_p$ , and  $T_{\text{eff},p}$  from Bakos et al. (2010),  $R_p$ ,  $P_{\text{orb}}$ ,  $a$ , and  $e$  from Huber, Czesla & Schmitt (2017a,b),  $d$  from *Gaia*, age from Bonfanti, Ortolani & Nascimbeni (2016),  $P_{\text{rot}}$  from Béky et al. (2014). HD 97658: All from Van Grootel et al. (2014), except  $d$  (*Gaia*), age (Bonfanti et al. 2016),  $P_{\text{rot}}$  (Henry et al. 2011),  $R_p$  and  $P_{\text{orb}}$  (Knutson et al. 2014). HD 149026: All from Southworth (2010) ( $P_{\text{rot}}$  from  $v \sin i$ ), except  $d$  (*Gaia*), and  $T_{\text{eff},*}$  (Sato et al. 2005). WASP-80: All from Triaud et al. (2013), except  $P_{\text{orb}}$  (Mancini et al. 2014) and  $P_{\text{rot}}$  from  $v \sin i$  (Triaud et al. 2015).


**Figure 1.** Distances and radii of all known transiting planets within 100 pc of the Earth. The six planets in our sample are shown as red squares. Other planets are shown as grey circles. Data taken from NASA Exoplanet Archive.

flux values was obtained with the filtered data set. The results presented here use the filtered data set in the spectral fitting process and subsequent analysis, however the light curve for HAT-P-11 presented in Section 4.1 uses the unfiltered data set in order to avoid large gaps.

### 3.1 Nearby sources

HD 149026 is not known to be a double-star system (Raghavan et al. 2006; Bergfors et al. 2013), but STScI Digitized Sky Survey (DSS) images show a nearby star at 20 arcsec distance north-east of HD 149026. The source is also present in 2MASS images (Skrutskie et al. 2006) and our OM data. In the multi-epoch DSS images HD 149026 displays a proper motion of 3.651 arcsec measured over a time period of 40 yr (Raghavan et al. 2006). The nearby source is not comoving, hence, we identified it as a background source.

DSS and 2MASS images contain a source 8 arcsec away from HAT-P-11. This object was identified as KOI-1289 by the *Kepler* mission, and later found to be a false positive due to a blended

signal from HAT-P-11.<sup>2</sup> KOI-1289 is 4.6 mag fainter than HAT-P-11 in the  $B$  band, and 6.3 mag fainter in the  $R$  band (Høg et al. 2000; Cutri et al. 2003; Monet et al. 2003). This is consistent with our findings: KOI-1289 is barely detected in OM. Comparison of the OM positions of both objects to their respective J2000 positions (Cutri et al. 2003; van Leeuwen 2007) reveals proper motion in different directions at different rates, and are thus not comoving.

WASP-80 also has a much fainter star located nearby (9 arcsec), as discussed in section 3.1 of Salz et al. (2015). They identify it as a background 2MASS source, 4 mag dimmer than WASP-80.

In all four cases, the detected X-rays are centred on the exoplanet host star, and there is no evidence for X-rays from the nearby object. They were therefore neglected in the following analysis.

## 4 X-RAY ANALYSIS AND RESULTS

An X-ray source was detected within 1.5 arcsec of the expected position of each target star. 15 arcsec extraction regions were used for all sources, with multiple circular regions on the same CCD chip used for background extraction, located as close to the source as possible beyond 30 arcsec.

### 4.1 X-ray light curves

We analysed the time dependence of the targets for two primary purposes. First, we check for strong stellar flares that could bias the measurements of the quiescent X-ray flux. Secondly, as shown in Table 2, four of our observations coincide with full planetary transits, and a fifth contains partial transit coverage. We examined our light curves for evidence of planetary transit features.

Fig. 2 displays the background-corrected light curves, co-added across the three EPIC detectors. The count rate of HD 149026 is too low to detect any variability. Of the other five observations, GJ 436 and WASP-80 show temporal variability at the  $3\sigma$  level when tested against a constant, equal to the mean count rate. HAT-P-11 also experiences variation, with a significance just below  $3\sigma$ . However, no strong flares are detected in any of the data, and none of the five observations covering a transit show any evidence of transit features in their light curves at this precision.

<sup>2</sup>Flagged as a false positive on the MAST Kepler archive: <https://archive.stsci.edu/kepler/>. Inspection of the light curves reveals a transit signal with the same period as HAT-P-11.

**Table 2.** Details of our *XMM-Newton* observations.

Target	ObsID	PI	Start time (TDB)	Exp. T (ks)	Start–Stop phase	Transit phase	PN filter	OM filter(s)	Ref.
GJ 3470	0763460201	Salz	2015-04-15 03:13	15.0	0.838–0.890	0.988–1.012	Medium	<i>U/UVW1/UVW2</i>	1
WASP-80	0764100801	Wheatley	2015-05-13 13:08	30.0	0.944–1.065	0.986–1.014	Thin	<i>UVW1</i>	2
HAT-P-11	0764100701	Wheatley	2015-05-19 13:13	28.5	0.967–1.035	0.990–1.010	Thin	<i>UVW2</i>	3
HD 97658	0764100601	Wheatley	2015-06-04 04:35	30.9	0.980–1.019	0.994–1.006	Medium	<i>UVW2</i>	4
HD 149026	0763460301	Salz	2015-08-14 19:19	16.7	1.009–1.077	0.977–1.023	Medium	<i>UVM2/UVW2</i>	5
GJ 436	0764100501	Wheatley	2015-11-21 01:40	24.0	0.949–1.063	0.992–1.008	Thin	<i>UVW1</i>	6

Start time and duration are given for EPIC-pn. References for the ephemerides: (1) Biddle et al. (2014); (2) Triaud et al. (2013); (3) Huber et al. (2017b); (4) Knutson et al. (2014); (5) Carter et al. (2009); (6) Lanotte et al. (2014).

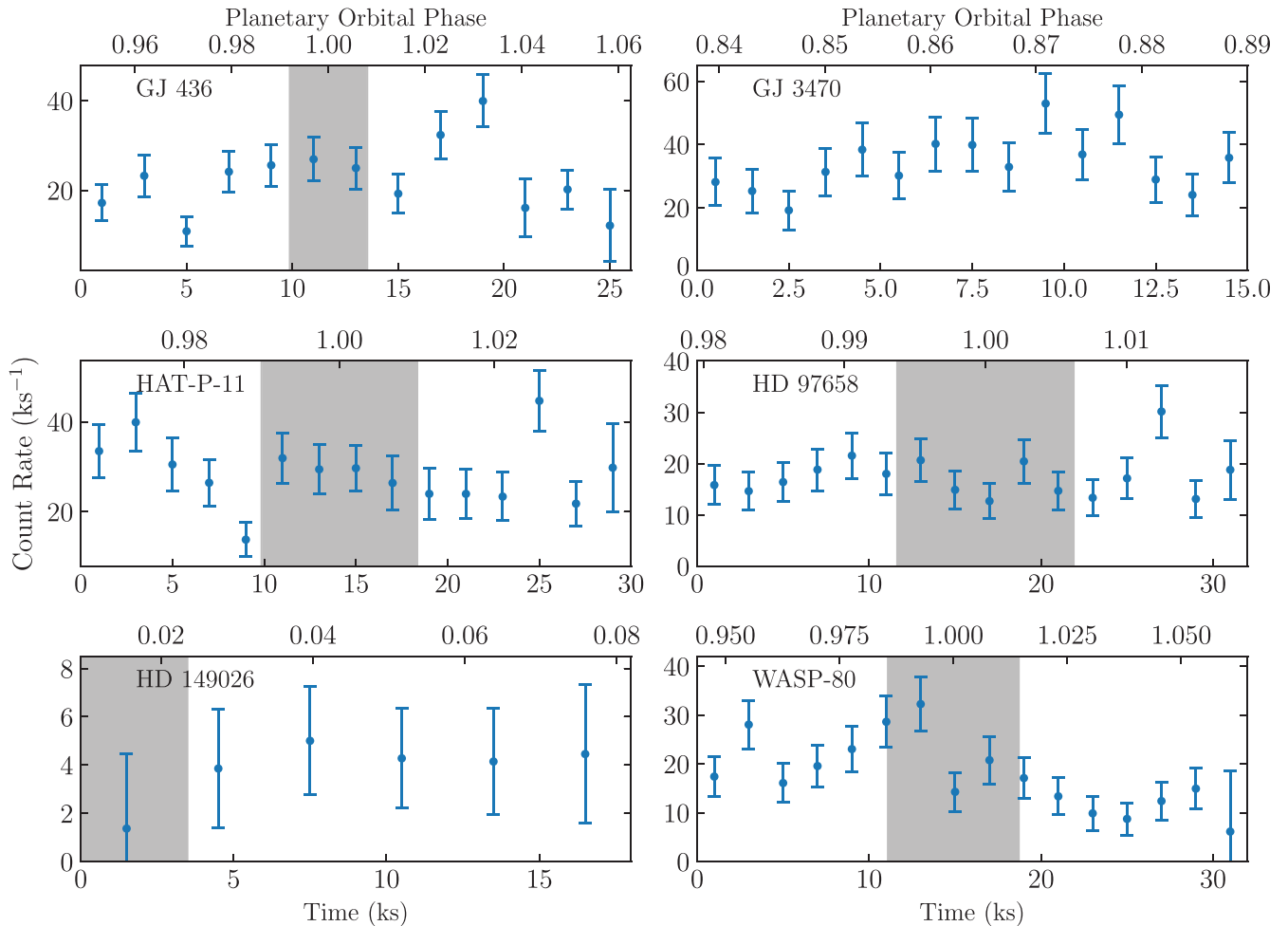


**Figure 2.** Background-corrected X-ray light curves of the six targets. The count rate is the sum of the three EPIC detectors. The areas shaded in grey are the planetary transits (1st to 4th contact) in visible light. Time in each case is that elapsed from the beginning of the observation, as listed in Table 2.

#### 4.2 X-ray spectra

We analysed the unbinned, background-corrected spectra in *XSPEC* 12.9.0 (Arnaud 1996). Accordingly, we used C-statistics in our subsequent model fitting (Cash 1979). The errors on our fitted parameter values were determined using *XSPEC*'s error command, with confidence intervals of 68 per cent.

We fitted APEC models for optically thin plasma in a state of collisional ionization equilibrium (Smith et al. 2001). In all cases with this model, a single-temperature fit can be rejected at 95 per cent confidence, using a Monte Carlo technique to assess the goodness

of fit. We therefore performed fits with two temperature components, which gives a good fit for all six data sets. The abundances were fixed to solar values (Asplund et al. 2009). Additionally, we included in a term for the interstellar absorption, making use of the TBABS model (Wilms, Allen & McCray 2000). We set the H I column density for GJ 436 and HD 97658 to the values found by Youngblood et al. (2016). For the other four objects we follow the approach of Salz et al. (2015), who fixed the H I column density to the distance of the system multiplied by a mean interstellar hydrogen density of 0.1 cm<sup>-3</sup> (Redfield & Linsky 2000). We note that this estimate applies only to the Local Interstellar Cloud, and is

not strictly applicable for lines of sight that contain other interstellar clouds. Redfield & Linsky (2008) showed that lines of sight to nearby stars varied around the average  $N_{\text{H}}$  value by about a factor of 3. We found that changing  $N_{\text{H}}$  by a factor of 3 in either direction only changes the best-fitting measured fluxes by a few per cent, well within the measured uncertainties.

The APEC-fitted EPIC-pn X-ray spectra are shown in Fig. 3. These have been binned to lower resolution to aid visualization. The X-ray fluxes at the Earth for the directly observed 0.2–2.4 keV band,  $F_{\text{X}, \oplus}$ , are shown in Table 3. To obtain the unabsorbed fluxes, we changed the H I column density to zero on the fitted model and reran the flux command. Since the error command cannot be run without refitting the model, we scaled the uncertainties so as to keep the percentage error constant between the absorbed and unabsorbed fluxes.

### 4.3 X-ray fluxes

Most commonly used energy ranges for X-ray fluxes in the literature are conventions resulting from the passbands of various observatories. The *ROSAT* band (0.1–2.4 keV; 5.17–124 Å) is one of the most widely employed. However, this band is not so easily applied to data from the current generation of X-ray observatories: the effective area of *XMM-Newton*'s EPIC-pn and *Chandra*'s ACIS-S both decline quickly below 0.25 keV. Thus, extrapolations to the *ROSAT* energy range must be made. As highlighted in Bourrier et al. (2017b) and Wheatley et al. (2017), while the fluxes obtained in XSPEC are usually seen to be consistent with one another in directly observed bands, the fluxes when extrapolated down to 0.1 keV can disagree significantly between models.

We investigated the extrapolation discrepancy between the APEC model and CEMEKL, the second model used by Bourrier et al. (2017b) and Wheatley et al. (2017). The latter is a multi-temperature plasma emission model, wherein the emission measure as a function of temperature is described by a power law (Schmitt et al. 1990; Singh, White & Drake 1996). The TBABS term accounting for interstellar absorption was applied in the same way as for the APEC model, above. For HD 97658, the CEMEKL model yields a flux in the 0.2–2.4 keV band of  $(2.90^{+0.15}_{-0.24}) \times 10^{-14} \text{ erg cm}^{-2} \text{ s}^{-1}$ , in good agreement with the APEC value of  $(2.92^{+0.16}_{-0.77}) \times 10^{-14} \text{ erg cm}^{-2} \text{ s}^{-1}$ . However, when extrapolated down to 0.1 keV, the CEMEKL value,  $1.34 \times 10^{-13} \text{ erg cm}^{-2} \text{ s}^{-1}$ , was almost four times lower than the corresponding APEC value of  $5.3 \times 10^{-13} \text{ erg cm}^{-2} \text{ s}^{-1}$ . Similar, but smaller, differences were also observed for the other objects. These originate from the different temperature-emission measure distribution assumptions of the models. For this reason, we chose to extrapolate directly from the observed X-ray fluxes to the full XUV band, rather than taking a two-step method of extrapolating to the *ROSAT* band and then the EUV.

### 4.4 EUV reconstruction

EUV fluxes of stars must be reconstructed using other spectral ranges. Salz et al. (2015) compared three such methods, finding them to differ by up to an order of magnitude in active stars. However, Chadney et al. (2015), hereafter C15, presented a new empirical method of reconstructing the EUV flux from the measured X-ray flux. This method shows a better agreement with stellar rotation-based and stellar Ly  $\alpha$  luminosity-based reconstructions (Lecavelier Des Etangs 2007; Linsky et al. 2014) than the X-ray-based method of Sanz-Forcada et al. (2011).

C15 analysed observations of the Sun, deriving a power-law relation between the ratio of EUV to X-ray flux and the X-ray flux. This method seems physically well motivated, relating the fluxes at the stellar surface, thereby implicitly taking the local conditions of this region into account. Indeed, their result agrees well with synthetic spectra for a small number of nearby, K and M dwarf stars, as generated from coronal models. These synthetic spectra, in turn, agree with EUVE measurements within the uncertainties.

The C15 relation adopts the *ROSAT* band. Accordingly, they define the EUV band as 0.0136–0.1 keV (124–912 Å). As discussed in Section 4.3, this definition does not transfer well on to the current generation of X-ray telescopes. To apply the C15 relation to observations by either *XMM-Newton* or *Chandra*, one must perform two extrapolations. The first estimates the missing X-ray flux down to 0.1 keV, which we have shown to be uncertain by a factor of a few. The second occurs in applying the relation itself. Given the model dependence on the first of these steps highlighted above, it would be preferable to derive a new set of relations that allow direct extrapolation from the observed band to the rest of the XUV range in a single step. By reperforming the C15 analysis with different boundaries, we can derive such new relations that are more applicable to current instruments.

#### 4.4.1 Derivation of new X-ray–EUV relations

The data used by C15 come from the ongoing *TIMED/SEE* mission (Woods et al. 2005). One of the primary data outputs of the mission is daily averaged Solar irradiances, given in 10 Å intervals from 5 to 1945 Å. We integrated the fluxes up to the Lyman limit (0.0136 eV, 912 Å), splitting the data into X-ray and EUV bands either side of some defined boundary. Here, we used a range of boundary choices to produce our set of relations.

Using only the C15 sample (2002 May 30 to 2013 November 16), we were able to replicate their relation exactly, but we have the benefit of extra data. However, we noticed that some of the most recent observations appear to be offset from the rest of the data (see Fig. 4). This offset is likely a result of instrument degradation, which is not yet properly accounted for in the recent data (private communication with the *TIMED/SEE* team). Therefore, we chose to cut off all data past 2014 July 1, where the data start to show significant differences to older observations.

Additionally, we noticed that the errorbars in the merged file of all observations did not match those in the individual daily files, which was kindly fixed by the mission team. It seems that the data used by C15 had the same problem, so we also update C15's relation for the 0.1 keV boundary.

Fig. 5 shows the solar *TIMED/SEE* data and fluxes from the comparison synthetic stellar spectra, plotted for three of the boundary choices. The residuals of the single power-law fit reveal a trend. As the choice of boundary energy is increased, the log–log plot increasingly deviates from linear. A more complex function may be justified when solely considering the solar data. However, this would have proved less robust when extrapolating the relation to higher flux levels in active stars. We obtained synthetic spectra for a sample of nearby stars:  $\epsilon$  Eri from the X-Exoplanets archive,<sup>3</sup> and the spectra for AD Leo and AU Mic presented in C15. Using

<sup>3</sup>Available at <http://sdc.cab.inta-csic.es/xexoplanets/jsp/homepage.jsp>. See also Sanz-Forcada et al. (2011).

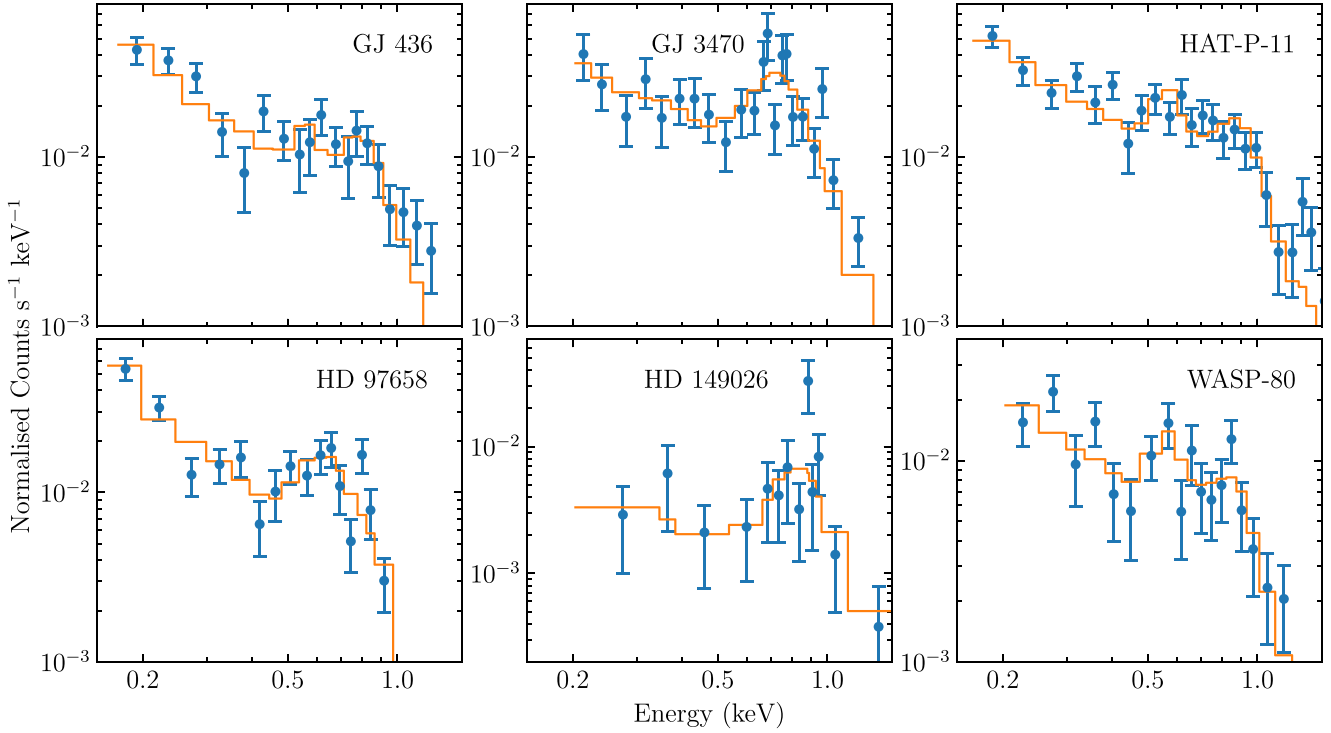


**Figure 3.** EPIC-pn X-ray spectra for the six targets. Unlike in the main analysis, the spectra are binned to a lower resolution to aid inspection. The background-corrected count rates are shown by the points with errorbars, with the histogram representing the fitted two-temperature APEC model.

**Table 3.** Results from our X-ray and EUV reconstruction analyses. The results given are for the X-ray range 0.2–2.4 keV, and corresponding EUV range 0.0136–0.2 keV. The X-ray fluxes at the Earth are the APEC modelled values.

System	$kT$ keV	$N_H$ (a)	EM (b)	$F_{X,\oplus}$ (c)	$L_X$ (d)	$L_{EUV}$ (d)	$F_{XUV,p}$ (e)	$F_{XUV,1\text{ au}}$ (e)	$L_{Ly\alpha}^\dagger$ (d)	$F_{Ly\alpha,\oplus}^\dagger$ (c)	$F_{Ly\alpha,\oplus}$ (c)
GJ 436	$0.12 \pm 0.01$ $0.61 \pm 0.08$	1.1	$0.19 \pm 0.3$ $0.048^{+0.007}_{-0.006}$	$2.91^{+0.16}_{-0.27}$	$0.33^{+0.02}_{-0.03}$	$3.0^{+0.2}_{-0.3}$	$1380^{+100}_{-150}$	$1.16^{+0.12}_{-0.16}$	3	27	$20^*, 21^\S$
GJ 3470	$0.09 \pm 0.03$ $0.35^{+0.06}_{-0.03}$	8.9	$1.7^{+4.1}_{-0.9}$ $1.0^{+0.2}_{-0.2}$	$4.5^{+0.2}_{-0.9}$	$4.5^{+0.8}_{-1.2}$	$14.3^{+3.7}_{-4.9}$	$4900^{+1000}_{-1300}$	$6.7^{+1.4}_{-1.8}$	13	13	–
HAT-P-11	$0.16 \pm 0.01$ $0.81^{+0.12}_{-0.06}$	12	$2.7 \pm 0.2$ $0.91^{+0.11}_{-0.10}$	$3.58^{+0.17}_{-0.21}$	$6.2^{+0.3}_{-0.4}$	$22.2^{+2.5}_{-2.7}$	$3560^{+330}_{-350}$	$10.07^{+0.95}_{-1.04}$	36	21	–
HD 97658	$0.044^{+0.013}_{-0.008}$ $0.24 \pm 0.1$	2.8	$15^{+16}_{-10}$ $0.56 \pm 0.06$	$2.92^{+0.16}_{-0.78}$	$1.62^{+0.09}_{-0.43}$	$11.1^{+1.1}_{-3.3}$	$700^{+60}_{-190}$	$4.52^{+0.42}_{-1.25}$	22	39	$42^\ddagger, 91^\S$
HD 149026	$0.09^{+0.41}_{-0.06}$ $0.71^{+0.14}_{-0.09}$	24	$2.3^{+148.6}_{-2.3}$ $1.7^{+0.4}_{-0.2}$	$0.84^{+0.01}_{-0.21}$	$5.9^{+0.2}_{-1.5}$	$37^{+5}_{-11}$	$8300^{+900}_{-2100}$	$15.2^{+1.7}_{-3.9}$	52	7.4	–
WASP-80	$0.15 \pm 0.02$ $0.73 \pm 0.09$	19	$3.6^{+2.8}_{-2.0}$ $1.1^{+0.9}_{-0.6}$	$1.78^{+0.11}_{-0.16}$	$8 \pm 5$	$19 \pm 14$	$8900 \pm 4300$	$9.5 \pm 5.3$	31	7.3	–

Notes. <sup>a</sup> $10^{18} \text{ cm}^{-2}$  (column density of H).

<sup>b</sup> $10^{50} \text{ cm}^{-3}$

<sup>c</sup> $10^{-14} \text{ erg cm}^{-2} \text{ s}^{-1}$  (at the Earth, unabsorbed).

<sup>d</sup> $10^{27} \text{ erg s}^{-1}$

<sup>e</sup> $\text{erg cm}^{-2} \text{ s}^{-1}$

<sup>†</sup>Estimated using the relations between EUV and Ly  $\alpha$  fluxes at 1 au in Linsky et al. (2014).

\* As reconstructed from observation by Bourrier et al. (2016).

<sup>‡</sup> As reconstructed from observation by Bourrier et al. (2017b).

<sup>§</sup> As reconstructed by (Youngblood et al. 2016).

these, a single power law fitted to the solar data agrees well with the comparison stars. During this comparison process, we also found that unweighting the solar data actually provided a slightly better fit with regard to the comparison stars across the choice of boundary energies.

Given the choice of a single power law, each relation takes the form

$$\frac{F_{\text{EUV}}}{F_X} = \alpha (F_X)^\gamma, \quad (1)$$

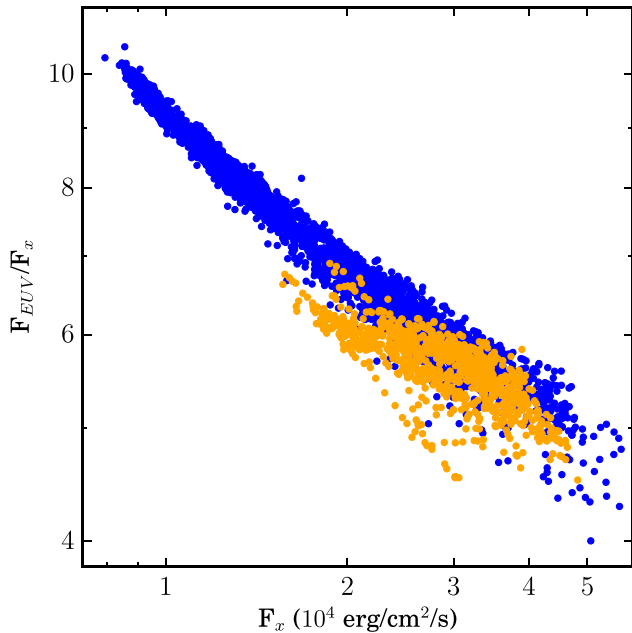


**Figure 4.** An updated version of fig. 2 of C15: the ratio of the EUV flux to X-ray flux plotted against the X-ray flux for a boundary energy of 0.1 keV. The C15 sample (2002 May 30 to 2013 November 16) is shown in blue, and data from 2013 November 17 to 2016 July 21 are shown in orange.

where  $F_{\text{EUV}}$  is the flux in the extrapolated band, from 0.0136 keV up to the chosen boundary, and  $F_X$  is the flux in the observed band, from the boundary up to 2.4 keV. The exception to this is the 0.124 keV boundary which, as per convention, extends the observed band to 2.48 keV. As in C15, these fluxes are those at the stellar surface. The values of  $\alpha$  and  $\gamma$  are given in Table 4 for each of the five boundary choices. As highlighted in Table 4, each of the boundary energies was chosen to correspond to the observational band of an X-ray satellite, or a widely used choice in the literature. We also include two further relations for going directly from the 0.2–2.4 keV band to the 0.0136–0.1 and 0.0136–0.124 keV EUV bands.

#### 4.4.2 Total XUV flux calculations

Using our newly derived relations, we determine the full XUV flux at the stellar surface, at the distance of each planet,  $F_{\text{XUV},p}$ , and at 1 au (see Table 3). For the zero eccentricity planets GJ 3470b and HD 149026b, we simply use the semimajor axis in Table 1. WASP-80b has a small upper limit on its eccentricity, so we again use the semimajor axis estimate. However, GJ 436, HAT-P-11, and HD 97658 all have non-zero eccentricities, and as such we use the time-averaged separation (see for a discussion, Williams 2003). Consequently, determined values of  $F_{\text{XUV},p}$  in these cases should also be considered time averages. We find that HD 149026b and WASP-80b are subject to the largest XUV irradiation. GJ 3470b and HAT-P-11b receive about half the XUV flux of HD 149026b and WASP-80b, but still a few times more than GJ 436b and HD 97658b.

Note that the XUV luminosity, and so  $F_{\text{XUV},p}$ , of WASP-80 are subject to larger uncertainty. This is a consequence of its poorly known distance of  $60 \pm 20$  pc (Triaud et al. 2013). No parallax was given in first *Gaia* data release, even though the star has a Tycho designation.

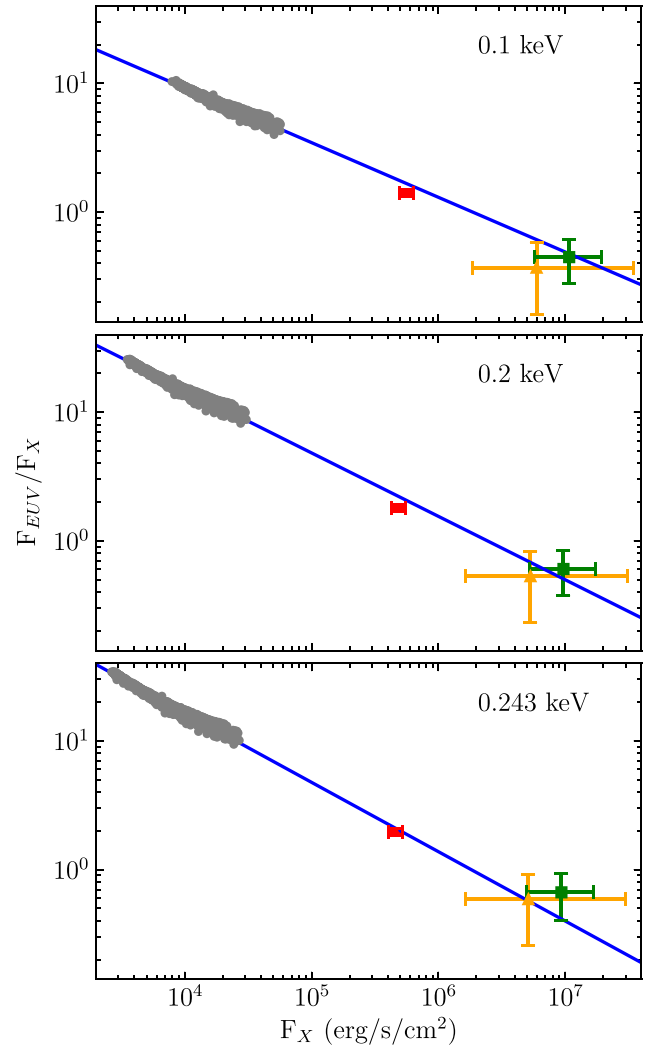


**Figure 5.** Solar *TIMED/SEE* data plotted for three of the new boundary energy choices: 0.1 keV/124 Å (top), 0.2 keV/62 Å (middle), and 0.243 keV/51 Å (bottom). Fluxes for the comparison stars are plotted as follows:  $\epsilon$  Eri – red circle; AD Leo – orange triangle; AU Mic – green square.

## 5 OM RESULTS

Observations using the OM camera on *XMM-Newton* were taken concurrently with those of the EPIC X-ray detectors. Different observing strategies were employed for this instrument in the two separate proposals that comprised the full set of observations we describe. In both cases, however, we have taken advantage of the NUV capabilities of the OM.

### 5.1 GJ 3470 and HD 149026

For GJ 3470 and HD 149026, some of the ultraviolet filters were cycled through in turn during the observation period. In the case of GJ 3470, all ultraviolet filters were employed except *UVW2*, which pushes furthest into the ultraviolet but is also the least sensitive. All ultraviolet filters were used for HD 149026, but the object was saturated in the *U* and *UVW1* filters, leaving useful measurements only for *UVW2* and the next bluest ultraviolet filter, *UVM2*.

For both objects, the measured count rates were converted into fluxes and magnitudes following the prescription of a *SAS* watchout

**Table 4.** Best-fitting power laws to be used in conjunction with equation (1) for the each choice of boundary energy. See Section 4.4.1.

#	X-ray range		EUV range		$\alpha$	$\gamma$	Relevant satellite
	(keV)	(Å)	(keV)	(Å)	( $\text{erg cm}^{-2} \text{s}^{-1}$ )		
1	0.100–2.400	5.17–124	0.0136–0.100	124–912	460	−0.425	<i>ROSAT</i> (PSPC)
2	0.124–2.480	5.00–100	0.0136–0.124	100–912	650	−0.450	None, widely-used (5–100 Å)
3	0.150–2.400	5.17–83	0.0136–0.150	83–912	880	−0.467	<i>XMM-Newton</i> (pn, lowest)
4	0.200–2.400	5.17–62	0.0136–0.200	62–912	1400	−0.493	{ <i>XMM-Newton</i> (pn, this work), <i>XMM-Newton</i> (MOS), <i>Swift</i> (XRT)}
5	0.243–2.400	5.17–51	0.0136–0.243	51–912	2350	−0.539	<i>Chandra</i> (ACIS)
6	0.200–2.400	5.17–62	0.0136–0.100	124–912	1520	−0.509	<i>XMM-Newton</i> (Observed to <i>ROSAT</i> EUV)
7	0.200–2.400	5.17–62	0.0136–0.124	100–912	1522	−0.508	<i>XMM-Newton</i> (Observed to 5–100 Å band)

**Table 5.** OM results for GJ 3470 and HD 149026.

Filter	Central $\lambda$ (Å)	Flux $10^{-15} \text{ erg cm}^{-2} \text{ s}^{-1} \text{ Å}^{-1}$	Mag.
<i>GJ 3470</i>			
<i>U</i>	3440	$3.66 \pm 0.07$	14.9
<i>UVW1</i>	2910	$0.49 \pm 0.24$	17.2
<i>UVM2</i>	2310	$1.2^a$	16.4
<i>HD 149026</i>			
<i>UVM2</i>	2310	$0.10 \pm 0.02$	19.1
<i>UVW2</i>	2120	$0.30 \pm 0.04$	18.1

Note. <sup>a</sup>Note that the UVM2 flux conversion introduces a factor of 2 error for M dwarf stars.

page.<sup>4</sup> We adopted the conversions for M0V and G0V stars for GJ 3470 and HD 149026, respectively (cf. spectral types in Table 1). The calculated fluxes and magnitudes for each filter used for each object are summarized in Table 5.

## 5.2 Fast mode observations

The other four objects were observed in a single filter, and in fast mode, in order to probe ultraviolet variation in the source over the course of the observation. This opened up the possibility of detecting the transit in the NUV. In each case, the single filter choice was a trade-off between wishing to push as far into the NUV as possible, while wanting to maintain a high enough (predicted) count rate that transit detection level precision might be possible. *UVW1* was chosen for GJ 436 and WASP-80, while HD 97658 and HAT-P-11 were observed using the *UVM2* filter.

The final light curves for GJ 436, HAT-P-11, and HD 97658 are shown in Fig. 6, and we conclude that none of these three observations detected the transit in NUV. The light curves were built by correcting the fast mode time series data from OMFCHAIN using the corresponding image mode extractions from OMICHAIN. The reasons for this are described in Appendix A.

### 5.2.1 WASP-80

We identified a possible transit detection in the WASP-80 data. Again, we correct the fast mode time series by the corresponding image mode extractions, as described in Appendix A.

<sup>4</sup>How can I convert from OM count rates to fluxes, available at <https://www.cosmos.esa.int/web/xmm-Newton/sas-watchout-uvflux>.

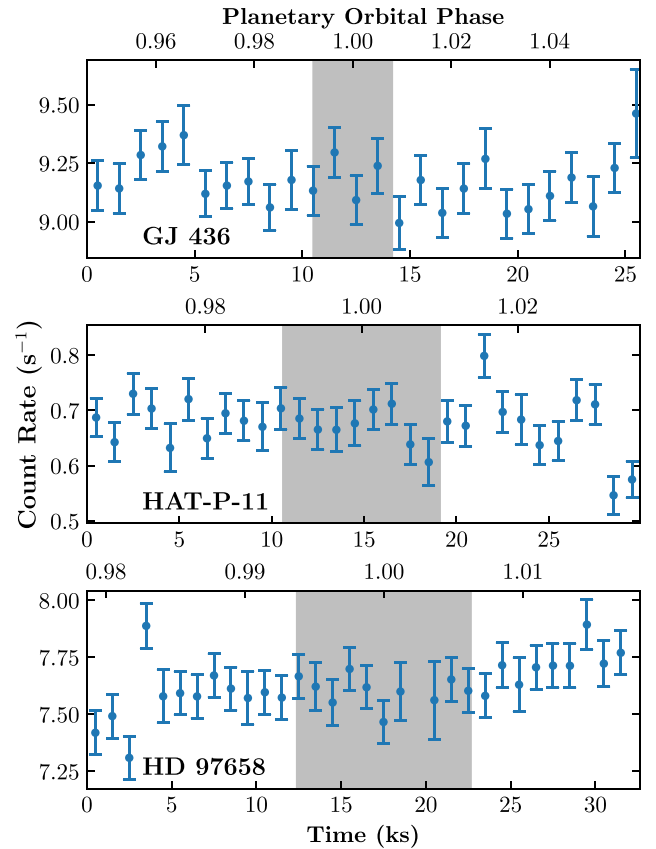


**Figure 6.** OM light curves for GJ 436, HAT-P-11, and HD 97658, binned to 1000 s resolution. The areas shaded in grey are the planetary transits (1st to 4th contact) in visible light.

We modelled our time series using the TRANSIT code,<sup>5</sup> a PYTHON implementation of the Mandel & Agol (2002) analytic transit model. To fit the model we used the MCMC sampler provided by the EMCEE package (Foreman-Mackey et al. 2013). We set Gaussian priors on the transit centre time,  $a/R_*$ , and the system inclination,  $i$ , according to the values and references in Tables 1 and 2. The prior for the transit centre at the epoch of our observations,  $t_{\text{Cen}}$ , was calculated using the ephemeris of Mancini et al. (2014).  $R_p/R_*$  and the out of

<sup>5</sup>Available as part of the RAINBOW package (<https://github.com/StuartLittlefair/rainbow>). Documentation can be found at <http://www.lpl.arizona.edu/~ianc/python/transit.html>.

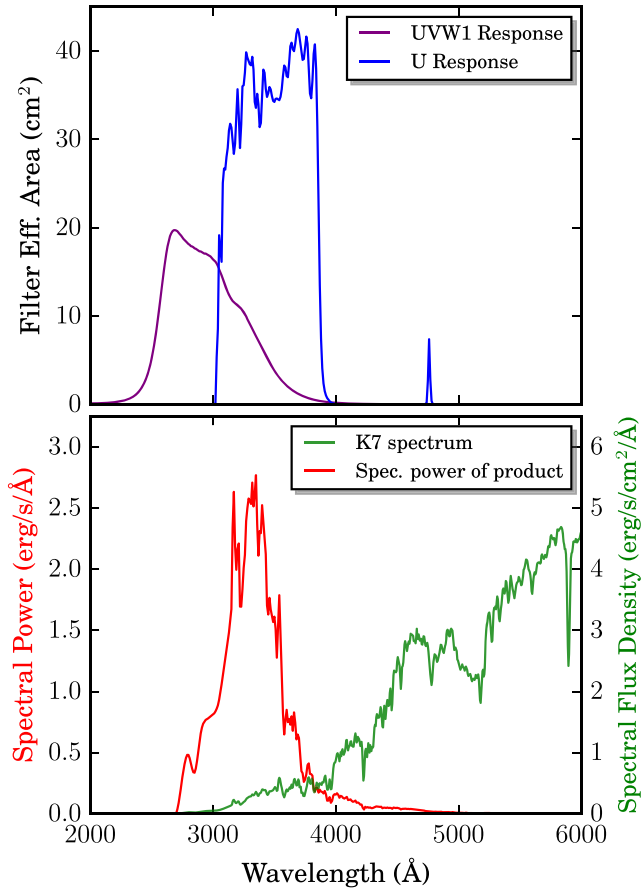


**Figure 7.** Top: Effective area of the *UVW1*- (purple) and *U*- band filters on the OM camera as a function of wavelength. Bottom: Model spectrum for a K7V star, and the product of the *UVW1* effective area and the K7V spectrum.

transit count rate were allowed to vary freely with uniform priors. The latter was included to normalize the out of transit data to an intensity of unity.

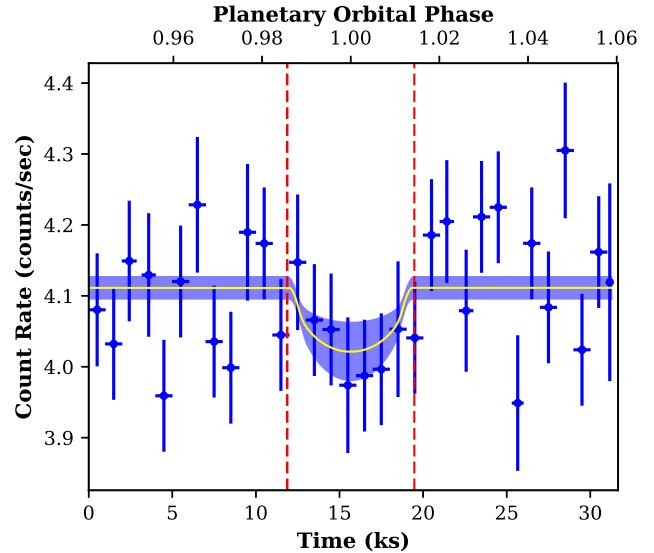
The limb darkening coefficients were fixed to those for the *U* band from Claret & Bloemen (2011), according to the stellar properties of WASP-80. Despite being taken with the *UVW1* filter, the sampling of the late-K dwarf spectrum is weighted to the *U* band, due to the red leak of the filter. This is shown in Fig. 7 which plots the effective area of the OM *UVW1*- and *U*-band filters, a model spectrum for a K7 dwarf star (Pickles 1998), and the product of the *UVW1* response with the model spectrum.

Fig. 8 displays the WASP-80 OM light curve with the best-fitting model and the  $1\sigma$  credibility region, with the data binned to a lower resolution to aid the eye. The resulting best-fitting parameters for the model are given in Table 6. The best-fitting depth is shallower than previous optical measurements, but is consistent to within  $1.6\sigma$ . Our best-fitting  $R_p/R_*$  shows some weak correlation with the out of transit count rate. The associated corner plot, made using the corner.py code (Foreman-Mackey 2016), is shown in Fig. 9.

## 6 DISCUSSION

### 6.1 X-ray Fluxes

The link between coronal X-ray emission and rotation period has been explored extensively (e.g. Pallavicini et al. 1981; Pizzolato



**Figure 8.** WASP-80 data binned to 1000 s bins. Overlaid is the best-fitting model (yellow) along with the  $1\sigma$  confidence region (blue shaded region). The dotted red lines correspond to the first and fourth contact of the transit, as calculated from the visible light ephemeris (Mancini et al. 2014).

**Table 6.** WASP-80 NUV MCMC fit priors and results.

Parameter	Value	Reference
<i>Gaussian priors</i>		
$t_{\text{Cen}}$ (BJD)	2457156.21885(31)	Mancini et al. (2014)
$a/R_*$	$12.989 \pm 0.029$	Triaud et al. (2013)
$i$	$89.92 \pm 0.10$	Triaud et al. (2013)
<i>Fixed values</i>		
$u1$	0.9646	Claret & Bloemen (2011)
$u2$	-0.1698	Claret & Bloemen (2011)
<i>Free, fitted parameter</i>		
$R_p/R_*$	$0.125^{+0.029}_{-0.039}$	<i>This work</i>

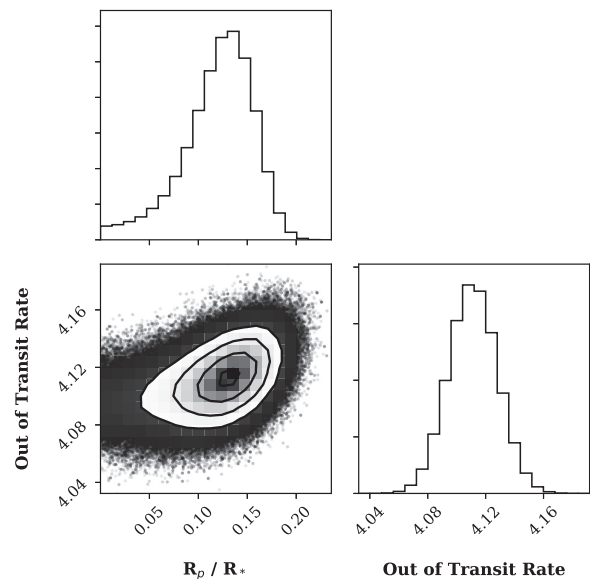


**Figure 9.** Corner plot for the WASP-80 fit showing the correlation of the out of transit count rate with  $R_p/R_*$ . The parameters bound by a Gaussian prior are omitted.

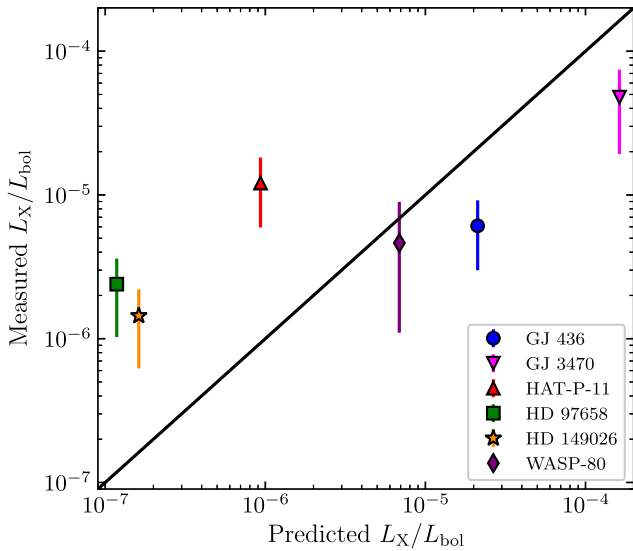


**Figure 10.** Comparison of the measured  $L_X/L_{\text{bol}}$  to that expected from the relations of **W11**.

et al. 2003; Wright et al. 2011; Jackson, Davis & Wheatley 2012; Stelzer et al. 2016; Wright & Drake 2016). At the shortest rotation periods, i.e. early in a star’s life, the X-ray emission is close to saturation, where the ratio of the X-ray emission to the bolometric luminosity,  $L_X/L_{\text{bol}}$ , is about  $10^{-3}$ . The rotation period,  $P_{\text{rot}}$ , of a star slows down as it ages. Once the rotation slows to beyond some critical value,  $L_X/L_{\text{bol}}$  is seen to drop off with a power-law behaviour.

Pizzolato et al. (2003) derived empirical relations describing  $L_X$  and  $L_X/L_{\text{bol}}$  as a function of  $P_{\text{rot}}$ . Further, they confirmed a relationship with Rossby number,  $R_o$ , for late-type stars with different convection properties.  $R_o$  is defined as the ratio of  $P_{\text{rot}}$  and  $\tau$ , the convective turnover time (Noyes, Weiss & Vaughan 1984). Wright et al. (2011), hereafter **W11**, formulated a set of empirical relations for this link between  $L_X/L_{\text{bol}}$  and  $R_o$ . This alternative formulation of the relationship reduced the scatter among unsaturated stars. **W11** also better constrain M stars due to their larger sample of such stars. This is useful for our study, which contains two M stars and a third on the K–M-type boundary. Wright & Drake (2016) further explored the application of this relation to low-mass, fully convective stars with their observed  $L_X/L_{\text{bol}}$  correlating well with the **W11** relations. We compare our measured fluxes to the **W11** relations.

The X-ray emission considered in **W11** is for the 0.1–2.4 keV *ROSAT* band. Examining the solar *TIMED/SEE* data in a similar way to the method in Section 4.4.1 with the two bands defined as 0.1–0.2 and 0.2–2.4 keV showed an approximate 1:1 ratio of flux in the two bands. We therefore doubled the flux in the observed 0.2–2.4 keV to estimate that in the *ROSAT* band. However, we added 50 per cent uncertainties in quadrature with the observed flux errors, due to the scatter of the comparison stars to the *TIMED/SEE* data.  $L_{\text{bol}}$  was evaluated using the Stefan–Boltzmann law. We note that the subgiant nature of HD 149026 means that the **W11** relations, derived for main-sequence stars, may not be directly applicable to the star.

Fig. 10 depicts our measured  $L_X/L_{\text{bol}}$  against that expected from **W11**. We note that our sample has a trend with slow rotators being more X-ray luminous than predictions, suggesting their activity may not drop as quickly as predicted. Booth et al. (2017) recently found a steeper age–activity slope for old, cool stars to previous studies. They suggested that in the context of the findings of van Saders

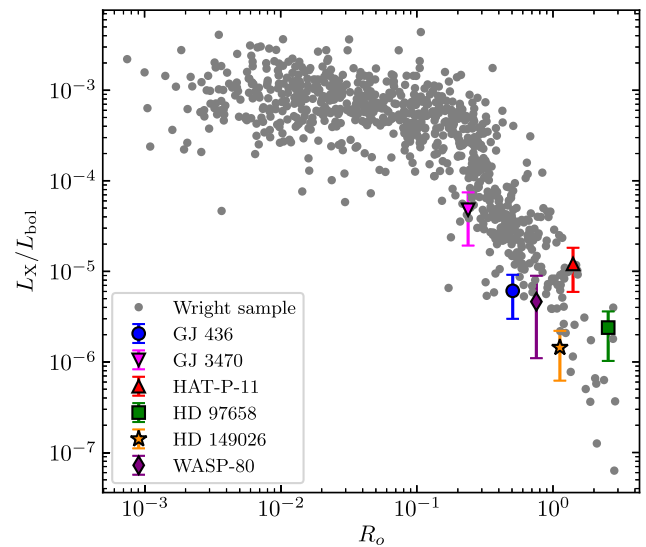


**Figure 11.** Replotting of fig. 1 of Wright & Drake (2016), itself an update of the **W11** sample, with points added from our own sample.

**Table 7.** Comparison of GJ 436 and WASP-80 X-ray fluxes with previous studies, grouped by energy range.

Data set	Reference	Energy range (keV)	Flux (a)
<i>GJ 436</i>			
2008, <i>XMM</i>	SF11	0.124–2.48	0.73
2008, <i>XMM</i>	E15	0.124–2.48	4.6
2008, <i>XMM</i>	This work	0.2–2.4	$2.26^{+0.11}_{-0.38}$
2015, <i>XMM</i>	This work	0.2–2.4	$2.91^{+0.16}_{-0.27}$
2008, <i>XMM</i>	E15	0.243–2.0	1.84
2013–14, <i>Chandra</i>	E15	0.243–2.0	1.97
2015, <i>XMM</i>	This work	0.243–2.0	$2.35^{+0.16}_{-0.26}$
<i>ROSAT</i> All-Sky Survey	H99, B16	0.1–2.4	<12
<i>WASP-80</i>			
2014, <i>XMM</i>	S15	0.124–2.48	$1.6^{+0.1}_{-0.2}$
2014, <i>XMM</i>	This work	0.2–2.4	$1.67^{+0.12}_{-0.26}$
2015, <i>XMM</i>	This work	0.2–2.4	$1.78^{+0.11}_{-0.16}$

a  $10^{-14}$  erg  $\text{cm}^{-2}$   $\text{s}^{-1}$  (at the Earth, unabsorbed).

References are: SF11: Sanz-Forcada et al. (2011); E15: Ehrenreich et al. (2015); H99: Hünsch et al. (1999); S15: Salz et al. (2015); B16: Boller et al. (2016).

et al. (2016), who found evidence for weaker magnetic braking in field stars older than 1 Gyr, this could point to a steepening of the rotation–activity relationship, in contrast to our measurements. Despite the apparent shallower trend in Fig. 10, our measurements are in line with the scatter in the **W11** sample itself, as can be seen in Fig. 11. The significant scatter in these activity relations underlines the need for measurements of X-ray fluxes for individual exoplanet hosts.

### 6.1.1 GJ 436

We compare our measured fluxes to previous studies. A summary of these comparisons can be found in Table 7.

GJ 436 previously had X-ray fluxes measured by Sanz-Forcada et al. (2011) and Ehrenreich et al. (2015) (hereafter E15) using the *XMM-Newton* data set from 2008 (Obs ID: 0556560101; PI: Wheatley). The two analyses produced very different results, with the former finding the flux at the Earth to be  $7.3 \times 10^{-15} \text{ erg cm}^{-2} \text{ s}^{-1}$  for the 0.124–2.48 keV band, almost five times smaller than the  $4.6 \times 10^{-14} \text{ erg cm}^{-2} \text{ s}^{-1}$  found by the latter analysis in the same energy range. We note that Louden et al. (2017) found a similar discrepancy between their analysis and that of Sanz-Forcada et al. (2011) for an observation of HD 209458. We reanalysed the previous *XMM-Newton* data set for GJ 436 for a more direct comparison of the fluxes, obtaining a flux of  $(2.26_{-0.38}^{+0.11}) \times 10^{-14} \text{ erg cm}^{-2} \text{ s}^{-1}$  in the 0.2–2.4 keV band. We therefore conclude that there was a modestly increased X-ray output at the time of the 2015 observations. GJ 436 was one of the stars whose light curve was seen to vary at the  $3\sigma$  level in Section 4.1. The difference in flux between the 2008 and 2015 data sets points to significant variation also on longer time-scales.

E15 also found their analysis of the 2008 *XMM-Newton* observations to agree with their *Chandra* data in the overlapping 0.243–2.0 keV energy range:  $1.84 \times 10^{-14} \text{ erg cm}^{-2} \text{ s}^{-1}$  versus the  $1.97 \times 10^{-14} \text{ erg cm}^{-2} \text{ s}^{-1}$  obtained when averaging across the four *Chandra* data sets. We measure  $(2.35_{-0.26}^{+0.16}) \times 10^{-14} \text{ erg cm}^{-2} \text{ s}^{-1}$  in this slightly more restrictive band, again showing a modest increase on the 2008 *XMM-Newton* data, but also compared to the averaged 2013–14 *Chandra* data. Furthermore, we compared the emission measures of the 2015 data to the other *XMM-Newton* and *Chandra* observations using the method of E15 (The results for the other five data sets are plotted in their extended data fig. 8). For the most direct comparison, we fixed the temperatures and abundances to that found in E15 (i.e. *not* those in Table 3). With this method, we obtain emission measures of  $(9.7_{-1.2}^{+1.3}) \times 10^{49}$  and  $(2.10_{-0.22}^{+0.23}) \times 10^{49} \text{ cm}^{-3}$  for the low- and high-temperature components, respectively. These results concur with the conclusion of E15 that there is more variation in the higher temperature component than in the soft.

We note that GJ 436 was also observed in X-rays during the *ROSAT* All-Sky Survey. Hünsch et al. (1999) reported an X-ray flux in the 0.1–2.4 keV band of  $1.2 \times 10^{-13} \text{ erg cm}^{-2} \text{ s}^{-1}$ , which is much higher than all of the other data sets. However, the revised PSPC catalogue by Boller et al. (2016) suggests the GJ 436 detection is not real and should be treated as an upper limit.

### 6.1.2 HAT-P-11

Morris et al. (2017) used Ca II H and K observations to show HAT-P-11 has an unexpectedly active chromosphere for a star of its type. Our work suggests this extends to the corona too, with its measured  $L_X/L_{\text{bol}}$  an order of magnitude larger than that expected from W11 (Fig. 10). Morris et al. (2017) also presented evidence for an activity cycle for HAT-P-11 in excess of 10 yr using observations of chromospheric emission, with the star’s S-index spending a greater proportion of its activity cycle close to maximum compared to the Sun. Despite this, our *XMM-Newton* observations were taken about halfway between activity maximum and minimum, and  $L_X/L_{\text{bol}}$  was much larger than the W11 prediction even though the star was not close to its maximum activity level.

### 6.1.3 WASP-80

WASP-80 has had a previous *XMM-Newton* data set from 2014 (Obs ID: 0744940101; PI: Salz) analysed by Salz et al. (2015).

They reported a flux at the Earth of  $(1.6_{-0.2}^{+0.1}) \times 10^{-14} \text{ erg cm}^{-2} \text{ s}^{-1}$ , in the 0.124–2.48 keV band. As for GJ 436, we repeated the analysis of this older data set using the same procedure as for the new observations for a more direct comparison. The fluxes can be compared in Table 7. We find a flux at the Earth in the slightly more restrictive 0.2–2.4 keV band of  $(1.67_{-0.26}^{+0.12}) \times 10^{-14} \text{ erg cm}^{-2} \text{ s}^{-1}$ . This result is consistent with our observations at the newer epoch within the uncertainties.

## 6.2 EUV estimation

In Section 4.4, we derived new empirical relations for reconstructing the EUV emission of stars from their observed X-rays, with the results presented in Table 3. We now draw comparisons to past applications of other methods.

For GJ 436, E15 obtained estimates of the EUV at 1 au from both the C15 X-ray and Linsky et al. (2014) Ly  $\alpha$  methods, and found them to be remarkably similar. Adjusting for the new distance estimate from *Gaia*, these were 0.92 and 0.98  $\text{erg cm}^{-2} \text{ s}^{-1}$ , respectively. In order to procure a directly comparable flux from our own measurements, we used equation (1) (with boundary energy choice #7 from Table 4). This was applied to our flux measurement from the same 2008 data set analysed by E15 (Section 6.1.1). We determine an EUV flux at 1 au of  $0.86_{-0.17}^{+0.06} \text{ erg cm}^{-2} \text{ s}^{-1}$ , in satisfactory agreement with the values found by E15. The corresponding EUV flux value for the new 2015 data set is  $0.98_{-0.12}^{+0.08} \text{ erg cm}^{-2} \text{ s}^{-1}$ .

Bourrier et al. (2016) also estimated the EUV flux using the Linsky et al. (2014) method. They determine EUV fluxes of 0.88 and 0.86  $\text{erg cm}^{-2} \text{ s}^{-1}$  at their two, independent epochs, in good agreement with our results from X-rays.

The MUSCLES Treasury Survey has combined observations from multiple passbands from X-ray to mid-IR to study the intrinsic spectral properties of nearby low-mass planet-hosting stars (France et al. 2016). Youngblood et al. (2016) reconstructed the EUV flux of GJ 436 in the 0.0136–0.1 keV band with the Linsky et al. (2014) Ly  $\alpha$  method, obtaining 0.83  $\text{erg cm}^{-2} \text{ s}^{-1}$  at 1 au. Their results are therefore also consistent with extrapolation from the X-ray band.

The data presented here for HD 97658 (Table 3) were previously investigated by Bourrier et al. (2017b). Unlike here, they first extrapolated to the *ROSAT* band, and then used C15 to extrapolate to the EUV. They also estimate the EUV from multiple epochs of *HST* Ly  $\alpha$  observations, applying the relations of Linsky et al. (2014). The results from the two methods were compatible. Our direct extrapolation to the EUV from the observed X-rays obtains an XUV flux at the planet that is marginally smaller, but consistent within the uncertainties to their best estimate. The agreement with EUV estimates from Ly  $\alpha$  supports the accuracy of the two methods of reconstructing the EUV emission.

## 6.3 Mass-loss rates

We present estimated mass-loss rates for all six planets in Table 8. We follow the energy-limited approach of previous studies (e.g. Lecavelier Des Etangs 2007; Sanz-Forcada et al. 2011; Salz et al. 2015; Louden et al. 2017; Wheatley et al. 2017) to calculate mass-loss rate estimates for each of the six systems:

$$\dot{M} = \frac{\beta^2 \eta \pi F_{\text{XUV}} R_p^3}{G K M_p}, \quad (2)$$

where  $\eta$  is the efficiency of the mass-loss,  $F_{\text{XUV}}$  is the total X-ray and EUV flux incident on the planet, and  $\beta$  accounts for the increased

**Table 8.** Current mass-loss rate and total lifetime mass-loss estimates of the six planets in our sample for different assumed sets of  $\eta$  and  $\beta$ . The first listed  $\eta$  and  $\beta$  for each planet are taken from Salz et al. (2016); the second is a canonical value of  $\eta = 0.15$  and  $\beta = 1$ ; the third provides a lower limit on the mass-loss rates of these planets, motivated by Ly  $\alpha$  observations.

System	$\eta$	$\beta$	$\log \dot{M}$ ( $\text{g s}^{-1}$ )	Lifetime Const. <sup>a</sup>	Loss per cent J12 <sup>b</sup>
GJ 436	0.275	1.48	9.8	0.8	4.3
	0.15	1	9.2	0.2	1.0
	>0.01	1	>8.0	>0.01	>0.07
GJ 3470	0.135	1.77	10.7	4.3	9.3
	0.15	1	10.2	1.5	3.5
	>0.01	1	>9.0	>0.1	>0.2
HAT-P-11	0.229	1.61	10.3	2.3	8.8
	0.15	1	9.7	0.6	2.4
	>0.01	1	>8.6	>0.04	>0.2
HD 97658	0.288	1.75	9.4	1.7	3.9
	0.15	1	8.6	0.3	0.7
	>0.01	1	>7.4	>0.02	>0.05
HD 149026	0.093	1.26	9.4	0.014	0.2
	0.15	1	9.4	0.015	0.2
	>0.01	1	>8.2	>0.001	>0.01
WASP-80	0.100	1.24	10.3	0.004	0.06
	0.15	1	10.3	0.004	0.05
	>0.01	1	>9.2	>0.0004	>0.004

Notes. <sup>a</sup>Constant lifetime XUV irradiation rate, at the current level.

<sup>b</sup>Lifetime XUV irradiation estimated by the relations of Jackson et al. (2012).

size of the planetary disc absorbing XUV photons compared to visible wavelengths, equal to  $R_{\text{XUV}}/R_p$ . We follow the approach of Salz et al. (2016), outlined in their footnote 1, in using a  $\beta^2$  factor (Watson, Donahue & Walker 1981; Lammer et al. 2003; Erkaev et al. 2007) instead of a  $\beta^3$  factor (e.g. Baraffe et al. 2004; Sanz-Forcada et al. 2010). The factor  $K$ , the potential energy difference between the surface and the Roche lobe height,  $R_{\text{RL}}$ , to which material must be lifted to escape, is given by (Erkaev et al. 2007)

$$K = 1 - \frac{3}{2\xi} + \frac{1}{2\xi^3}, \quad (3)$$

where  $\xi = R_{\text{RL}}/R_p$ . In turn, this can be approximated by  $(\delta/3)^{1/3}\lambda$  where  $\delta = M_p/M_*$ , and  $\lambda = a/R_p$ .

The value of  $\eta$  for a given system has been the subject of much discussion (e.g. Shematovich, Ionov & Lammer 2014; Loudon, Wheatley & Briggs 2017, and references therein), with estimates and adopted values often varying considerably from study to study (e.g. Penz et al. 2008; Murray-Clay et al. 2009; Owen & Jackson 2012). In Table 8 we estimate mass-loss rates corresponding to our observed XUV fluxes with three different assumptions for this efficiency. First, we make use of the results of coupled photoionization-hydrodynamic simulations by Salz et al. (2016), which included  $\eta$  and  $\beta$  values for all six planets in our sample. These calculations imply relatively high mass-loss efficiencies, especially for lower mass planets (Table 8). We also include a more canonical choice of 0.15 and 1 for  $\eta$  and  $\beta$ , respectively. These were the values adopted by Salz et al. (2015), allowing direct comparison of our predicted mass-loss rates with those systems. Our third assumption of 1 per cent efficiency is adopted as a lower limit to the likely mass-loss efficiency, and hence mass-loss rates, motivated by observational constraints from contemporaneous measurements of the XUV irradiation and resulting mass-loss detected through Ly  $\alpha$  absorption in

individual systems (e.g. Ehrenreich & Désert 2011). For GJ 436b an efficiency as low as 0.5 per cent has been shown to be sufficient to explain the observed strong Ly  $\alpha$  absorption, if the material is completely neutral as it leaves the planet (Ehrenreich et al. 2015; Bourrier et al. 2016). For the hot Jupiter HD 189733b a similarly low lower limit of 1 per cent is also sufficient to explain the observed absorption by H I, although a somewhat higher efficiency is likely to be needed to account for the unobserved ionized hydrogen (Lecavelier des Etangs et al. 2012). For the super-Earth HD 97658b, upper limits on Ly  $\alpha$  absorption from Bourrier et al. (2017b) suggest a mass-loss efficiency that could be substantially lower than that predicted by Salz et al. (2016), depending on the ionization fraction of material leaving the planet. Since this fraction is poorly known, the assumed value of 1 per cent efficiency in Table 8 provides a lower limit on the mass-loss rates of the planets. The true efficiency is likely to be higher, and indeed a much higher mass-loss efficiency is also required for HD 209458 (Louden et al. 2017). Given this uncertainty in the mass-loss efficiencies, we present mass-loss rates for all three choices of  $\eta$  and  $\beta$  in Table 8.

Following Salz et al. (2016), the mass-loss rate estimates for GJ 436b and HD 97658b exceed the values derived by modelling Ly  $\alpha$  observations with the EVAPORATING EXOPLANETS (EVE) code (Bourrier et al. 2016, 2017b). The resulting mass-loss estimates for the other choices of  $\eta$  and  $\beta$  for these planets are both lower and closer to their respective estimates from Ly  $\alpha$ , although the  $\eta = 0.01$  results perhaps provide a slight underestimation.

As discussed by Owen & Alvarez (2016), EUV-driven evaporation of close-in planets can be in one of three regimes: energy-limited, recombination-limited, and photon-limited. Their numerical calculations show that the transition between the three regimes does not occur at a single point, rather over a few orders of magnitude. However, their fig. 1 allows us to determine that GJ 3470b, HAT-P-11b, and HD 97658b are likely in the region of energy-limited escape. HD 149026b and WASP-80b lie close to the transition between the energy-limited and recombination-limited regions. Note that energy conservation always applies in the planetary thermospheres, but in the case of recombination-limited escape, a larger fraction of the absorbed radiative energy is re-emitted by recombination processes, so that less energy is available to drive the planetary wind. Therefore, the recombination-limited regime exhibits lower evaporation efficiencies than the energy-limited regime. In agreement with their intermediate location close to the recombination regime, the estimates of  $\eta$  for HD 149026b and WASP-80b from Salz et al. (2016) are smaller than for the other four planets.

### 6.3.1 Total lifetime mass-loss

Jackson et al. (2012) produced a set of relations characterizing the evolution of the X-ray emission with stellar age. As a result, they were able to further derive relations that can be used to estimate the total X-ray emission of a star over its lifetime to date. In turn, this could be used to estimate the total mass lost from an exoplanet. This would be particularly useful to apply to close-in super-Earth and mini-Neptune-sized planets, to investigate if they could have suffered substantial or total loss of a gaseous envelope. For middle-aged systems, if this happened, it is likely to have occurred much earlier in their life when the coronal emission of their host was much greater.

We apply equation (8) of Jackson et al. (2012), together with the ages from Table 1, in order to estimate the lifetime X-ray output from each of the six host stars in our sample. The results are given

in Table 8. Additionally, we consider the corresponding EUV by applying relation #1 (Table 4) to the estimated X-ray output at 1000 yr steps and integrating over the resulting lifetime evolution. We then scale the results to the average orbital separation of the system's planet, and apply equation (2) to estimate the total mass lost over the planet's lifetime. Estimates for all three sets of choices of  $\eta$  and  $\beta$  are included. Also in Table 8 are estimates for the total percentage mass-loss over the lifetime of each planet, assuming a constant XUV irradiation rate, at the current level. While we assume a constant radius across the planet's lifetime, if substantial evolution has occurred, the use of a constant radius could mask a greater total lifetime mass-loss than our estimates (Howe & Burrows 2015).

The lifetime loss results are sensitive to the assumed  $\eta$  and  $\beta$ , as well as discrepancies between the theoretically expected  $L_X/L_{\text{bol}}$  and that observed. Additionally, HD 149026's subgiant nature will affect its estimate. However, more qualitatively, the four smallest planets studied are expected to have lost a much greater percentage of their mass over their lifetime than the other two much larger planets in the sample.

Applying equation (2) to a planet of Neptune mass and radius with the same irradiation history as HD 97658b, we find such a planet would have lost  $\sim 3.5$  per cent of its mass over its lifetime. This is in contrast to closer-in planets like CoRoT-7b, which is suspected to have suffered a near-complete loss of its gaseous envelope due to intense irradiation (Jackson et al. 2010).

#### 6.4 Ly $\alpha$ estimation

Ly $\alpha$  observation of highly irradiated exoplanets is an important tool to determine the extent of atmospheric evaporation. Ly $\alpha$  transits have proven successful in detecting evaporating atmospheres. Additionally, as previously stated, Ly $\alpha$  observations also provide a separate regime from which EUV reconstruction can be performed.

For each of the systems in our sample, we have estimated the Ly $\alpha$  output in two steps. First, we used equation (1) (boundary relation #7) to calculate the EUV flux in the 0.0136–0.124 keV band. Then, we applied the relations of Linsky et al. (2014), linking Ly $\alpha$  and EUV fluxes at 1 au. By plotting the curves given by the relations, we approximated the Ly $\alpha$  flux according to the position of each systems' EUV estimation. Table 3 gives Ly $\alpha$  luminosity,  $L_{\text{Ly}\alpha}$ , estimates for our six systems, and the corresponding flux at the Earth,  $F_{\text{Ly}\alpha, \oplus}$ . For GJ 436 and HD 97658, we additionally include literature values. While the results from Bourrier et al. (2016) and Bourrier et al. (2017b) for GJ 436 are remarkably consistent with our results, there is less agreement with those of Youngblood et al. (2016) for HD 97658, although their value is poorly constrained with larger errors.

Our analysis suggests that the HAT-P-11 system is the best candidate for Ly $\alpha$  observations, of those that have not previously been studied in this way. We predict the star to have the largest apparent Ly $\alpha$  brightness of the three, while we estimate the planet's mass-loss rate to be larger than that of GJ 436b by about a factor of 3. This is largely because the observed X-ray flux is significantly higher than expected. While our  $F_{\text{Ly}\alpha, \oplus}$  prediction does account for interstellar absorption, the Ly $\alpha$  snapshot of WASP-80 by Salz (2015) shows that large transits could even be detected for one of the most distant systems in this sample. Hence, all of the studied systems likely qualify for systematic Ly $\alpha$  transit observations, but HAT-P-11 and GJ 3470 appear to be the best suited.

#### 6.5 WASP-80 NUV transit

The OM light curve of WASP-80 allowed us to detect the planetary transit in the NUV. Our best-fitting  $R_p/R_*$  of  $0.125_{-0.039}^{+0.029}$  corresponds to a NUV transit depth of  $1.6_{-0.7}^{+0.5}$  per cent, and a planet radius of  $0.69_{-0.22}^{+0.16} R_J$ . In comparison, the discovery paper reported a visible light  $R_p/R_*$  of  $0.17126_{-0.0026}^{+0.0031}$  (Triaud et al. 2013), while Mancini et al. (2014) measured  $0.17058 \pm 0.00057$ , and Kirk et al. (2018) found  $0.17113 \pm 0.00138$ . The latter study also found little evidence of large variation in the radius of WASP-80 b across the visible and near-infrared. Our results are consistent, though the best-fitting transit is shallower by  $1.59\sigma$ . This is perhaps a hint that the NUV transit is shallower, consistent with the single  $U$ -band transit observed by Turner et al. (2017). It would be desirable to follow up with more observations in the NUV that could constrain the depth to a higher precision, particularly given the size of the uncertainties on our fitted depth.

A shallower NUV transit would not be without precedent. With ground-based observations, Turner et al. (2016) found smaller NUV ( $U$  band) transit depths for hot Jupiters WASP-1b and WASP-36b with significance  $3.6\sigma$  and  $2.6\sigma$ , respectively. Physically, a shallower transit in NUV could result from the planet passing in front of dimmer regions of the star. The contrast between the areas of the stellar disc the planet crosses and brighter regions elsewhere would also need to be higher in the NUV than visible light for this explanation to be feasible. Unocculted faculae could possibly produce this effect. Spectral modelling of faculae has shown the contrast in intensity between the facula and elsewhere on the stellar disc is greater in the UV than in the visible and IR, as well as for regions closer to the limb of the disc (e.g. Unruh, Solanki & Fligge 1999; Norris et al. 2017). Indeed, stellar activity in the transit light curve of WASP-52 b was interpreted by Kirk et al. (2016) as occulted faculae. WASP-80 b has a much lower impact parameter than WASP-52 b, and so spends less time crossing regions close to the limb, making it more likely that high-contrast faculae close to the limb would go unocculted.

#### 7 CONCLUSIONS

We have analysed *XMM-Newton* data to investigate the XUV environments of six nearby transiting planets that orbit in close proximity to their host star, ranging in size from Jupiter-size to super-Earth. For each star, we directly measure the flux in the 0.2–2.4 keV band by fitting a two-temperature APEC model. We use a similar approach to Chadney et al. (2015) in using Solar *TIMED/SEE* data to derive a new set of relations for reconstructing the unobservable EUV emission. We use different boundary choices between the EUV and X-ray bands based on the current generation of X-ray instruments. The resulting estimates for the full XUV range of GJ 436 and HD 97658 are in good agreement with past reconstructions from X-ray and Ly $\alpha$ .

With the contemporaneous measurements from the OM in the NUV, we searched for transits in the fast mode data. We successfully uncovered a transit from OM data for the first time. Our resulting fit showed a best-fitting transit depth for WASP-80b consistent with previous studies in visible light and in the near-infrared within the uncertainties. However, there is a hint that the depth could be shallower, and so we recommend further observations in the NUV to investigate more precisely the possibility of a smaller transit depth at these wavelengths.

We investigated how our measured X-ray emission, and its ratio to the corresponding bolometric luminosity, compared to that expected

from the known rotation rate and estimated Rossby number of each star. We see a possible trend to slower rotating stars being brighter than expected. The scatter in these results highlights the importance of investigating systems of interest with dedicated observations.

The mass-loss rate for each planet was estimated. Our mass-loss rates for GJ 436b and HD 97658b calculated using the efficiency and absorption radii determined by Salz et al. (2016) appear inconsistent with analysis of Ly $\alpha$  observations. Based on our Ly $\alpha$  emission estimates, all six systems qualify for observations at those wavelengths. However, HAT-P-11b and GJ 3470b are best suited of the four without previous extensive investigation due to their proximity to the Solar system. Both systems have larger predicted mass-loss rates than GJ 436b or HD 97658b. Finally, we determine that the super-Earth and three Neptunes among our sample are likely to have lost a larger mass fraction over their lifetimes than the other two larger planets.

## ACKNOWLEDGEMENTS

We thank the referee, Jeffrey Linsky, for his helpful comments which improved the quality of this manuscript. We thank Don Woodraska for providing some clarifications with the *TIMED/SEE* data, and Jorge Sanz-Forcada for providing the synthetic spectra data for AD Leo and AU Mic. GWK and JK are supported in part by STFC studentships. PJW is supported by an STFC consolidated grant (ST/P000495/1). MS acknowledges support by the DFG SCHM 1032/57-1 and DLR 50OR1710. DE and VB acknowledge support from the National Centre for Competence in Research ‘Planets’ of the Swiss National Science Foundation (SNSF) and from the European Research Council (ERC) under the European Union’s Horizon 2020 research and innovation programme (project ‘FOUR ACES’; grant agreement no. 724427).

## REFERENCES

- Arnaud K. A., 1996, in Jacoby G. H., Barnes J., eds, ASP Conf. Ser. Vol. 101, *Astronomical Data Analysis Software and Systems V*. Astron. Soc. Pac., San Francisco, p. 17
- Asplund M., Grevesse N., Sauval A. J., Scott P., 2009, *ARA&A*, 47, 481
- Awiphan S. et al., 2016, *MNRAS*, 463, 2574
- Bakos G. Á. et al., 2010, *ApJ*, 710, 1724
- Ballester G. E., Ben-Jaffel L., 2015, *ApJ*, 804, 116
- Baraffe I., Selsis F., Chabrier G., Barman T. S., Allard F., Hauschildt P. H., Lammer H., 2004, *A&A*, 419, L13
- Beugé C., Nesvorný D., 2013, *ApJ*, 763, 12
- Ben-Jaffel L., Ballester G. E., 2013, *A&A*, 553, A52
- Bergfors C. et al., 2013, *MNRAS*, 428, 182
- Biddle L. I. et al., 2014, *MNRAS*, 443, 1810
- Boller T., Freyberg M. J., Trümper J., Haberl F., Voges W., Nandra K., 2016, *A&A*, 588, A103
- Bonfanti A., Ortolani S., Nascimbeni V., 2016, *A&A*, 585, A5
- Booth R. S., Poppenhaeger K., Watson C. A., Silva Aguirre V., Wolk S. J., 2017, *MNRAS*, 471, 1012
- Bourrier V., Ehrenreich D., King G., Lecavelier des Etangs A., Wheatley P. J., Vidal-Madjar A., Pepe F., Udry S., 2017b, *A&A*, 597, A26
- Bourrier V., Lecavelier des Etangs A., Ehrenreich D., Tanaka Y. A., Vidotto A. A., 2016, *A&A*, 591, A121
- Bourrier V. et al., 2013, *A&A*, 551, A63
- Bourrier V. et al., 2017a, *A&A*, 602, A106
- Bourrier V. et al., 2017c, *A&A*, 599, L3
- Bourrier V. et al., 2018, *Nature*, 553, 477
- Bowyer S., Malina R. F., 1991, *Adv. Space Res.*, 11, 205
- Béky B., Holman M. J., Kipping D. M., Noyes R. W., 2014, *ApJ*, 788, 1
- Carter J. A., Winn J. N., Gilliland R., Holman M. J., 2009, *ApJ*, 696, 241
- Cash W., 1979, *ApJ*, 228, 939
- Chadney J. M., Galand M., Unruh Y. C., Koskinen T. T., Sanz-Forcada J., 2015, *Icarus*, 250, 357 (C15)
- Claret A., Bloemen S., 2011, *A&A*, 529, A75
- Currie M. J., Berry D. S., Jenness T., Gibb A. G., Bell G. S., Draper P. W., 2014, in Manset N., Forshay P., eds, ASP Conf. Ser. Vol. 485, *Astronomical Data Analysis Software and Systems XXIII*. Astron. Soc. Pac., San Francisco, p. 391
- Cutri R. M. et al., 2003, The IRSA 2MASS All-Sky Point Source Catalog, NASA/IPAC Infrared Science Archive. Available at: <http://irsa.ipac.caltech.edu/applications/Gator/>
- Davis T. A., Wheatley P. J., 2009, *MNRAS*, 396, 1012
- Eaton N., Draper P. W., Allan A., 2009, Starlink User Note, 45
- Ehrenreich D., Désert J.-M., 2011, *A&A*, 529, A136
- Ehrenreich D. et al., 2012, *A&A*, 547, A18
- Ehrenreich D. et al., 2015, *Nature*, 522, 459 (E15)
- Erkaev N. V., Kulikov Y. N., Lammer H., Selsis F., Langmayr D., Jaritz G. F., Biernat H. K., 2007, *A&A*, 472, 329
- Fontenla J. M., Landi E., Snow M., Woods T., 2014, *Sol. Phys.*, 289, 515
- Foreman-Mackey D., 2016, *The Journal of Open Source Software*, 24
- Foreman-Mackey D., Hogg D. W., Lang D., Goodman J., 2013, *PASP*, 125, 306
- France K. et al., 2016, *ApJ*, 820, 89
- Gaia Collaboration, 2016, *A&A*, 595, A2
- Helled R., Lozovsky M., Zucker S., 2016, *MNRAS*, 455, L96
- Henry G. W., Howard A. W., Marcy G. W., Fischer D. A., Johnson J. A., 2011, preprint (arXiv:1109.2549)
- Howe A. R., Burrows A., 2015, *ApJ*, 808, 150
- Huber K. F., Czesla S., Schmitt J. H. M. M., 2017a, *A&A*, 597, A113
- Huber K. F., Czesla S., Schmitt J. H. M. M., 2017b, *A&A*, 600, C1
- Høg E. et al., 2000, *A&A*, 355, L27
- Hünsch M., Schmitt J. H. M. M., Sterzik M. F., Voges W., 1999, *A&AS*, 135, 319
- Jackson A. P., Davis T. A., Wheatley P. J., 2012, *MNRAS*, 422, 2024
- Jackson B., Miller N., Barnes R., Raymond S. N., Fortney J. J., Greenberg R., 2010, *MNRAS*, 407, 910
- Kirk J., Wheatley P. J., Loudon T., Littlefair S. P., Copperwheat C. M., Armstrong D. J., Marsh T. R., Dhillon V. S., 2016, *MNRAS*, 463, 2922
- Kirk J., Wheatley P. J., Loudon T., Skillen I., King G. W., McCormac J., Irwin P. G. J., 2018, *MNRAS*, 474, 876
- Knutson H. A. et al., 2011, *ApJ*, 735, 27
- Knutson H. A. et al., 2014, *ApJ*, 794, 155
- Lammer H., Selsis F., Ribas I., Guinan E. F., Bauer S. J., Weiss W. W., 2003, *ApJ*, 598, L121
- Lanotte A. A. et al., 2014, *A&A*, 572, A73
- Lavie B. et al., 2017, *A&A*, 605, L7
- Lecavelier Des Etangs A., 2007, *A&A*, 461, 1185
- Lecavelier Des Etangs A. et al., 2010, *A&A*, 514, A72
- Lecavelier des Etangs A. et al., 2012, *A&A*, 543, L4
- Linsky J. L., Fontenla J., France K., 2014, *ApJ*, 780, 61
- Linsky J. L., Yang H., France K., Froning C. S., Green J. C., Stocke J. T., Osterman S. N., 2010, *ApJ*, 717, 1291
- Lopez E. D., Fortney J. J., 2013, *ApJ*, 776, 2
- Loudon T., Wheatley P. J., Briggs K., 2017, *MNRAS*, 464, 2396
- Loyd R. O. P. et al., 2016, *ApJ*, 824, 102
- Mancini L. et al., 2014, *A&A*, 562, A126
- Mandel K., Agol E., 2002, *ApJ*, 580, L171
- Monet D. G. et al., 2003, *AJ*, 125, 984
- Morris B. M. et al., 2017, *ApJ*, 848, 58
- Murray-Clay R. A., Chiang E. I., Murray N., 2009, *ApJ*, 693, 23
- Norris C. M., Beech B., Unruh Y. C., Solanki S. K., Krivova N. A., Yeo K. L., 2017, *A&A*, 605, A45
- Noyes R. W., Weiss N. O., Vaughan A. H., 1984, *ApJ*, 287, 769
- Owen J. E., Alvarez M. A., 2016, *ApJ*, 816, 34
- Owen J. E., Jackson A. P., 2012, *MNRAS*, 425, 2931
- Pallavicini R., Golub L., Rosner R., Vaiana G. S., Ayres T., Linsky J. L., 1981, *ApJ*, 248, 279
- Penz T. et al., 2008, *Planet. Space Sci.*, 56, 1260

- Pickles A. J., 1998, *PASP*, 110, 863
- Pizzolato N., Maggio A., Micela G., Sciortino S., Ventura P., 2003, *A&A*, 397, 147
- Raghavan D., Henry T. J., Mason B. D., Subasavage J. P., Jao W.-C., Beaulieu T. D., Hambly N. C., 2006, *ApJ*, 646, 523
- Redfield S., Linsky J. L., 2000, *ApJ*, 534, 825
- Redfield S., Linsky J. L., 2008, *ApJ*, 673, 283
- Salz M., 2015, PhD thesis, Universität Hamburg
- Salz M., Schneider P. C., Czesla S., Schmitt J. H. M. M., 2015, *A&A*, 576, A42
- Salz M., Schneider P. C., Czesla S., Schmitt J. H. M. M., 2016, *A&A*, 585, L2
- Sanz-Forcada J., Micela G., Ribas I., Pollock A. M. T., Eiroa C., Velasco A., Solano E., García-Álvarez D., 2011, *A&A*, 532, A6
- Sanz-Forcada J., Ribas I., Micela G., Pollock A. M. T., García-Álvarez D., Solano E., Eiroa C., 2010, *A&A*, 511, L8
- Sato B. et al., 2005, *ApJ*, 633, 465
- Schmitt J. H. M. M., Collura A., Sciortino S., Vaiana G. S., Harnden Jr. F. R., Rosner R., 1990, *ApJ*, 365, 704
- Shematovich V. I., Ionov D. E., Lammer H., 2014, *A&A*, 571, A94
- Singh K. P., White N. E., Drake S. A., 1996, *ApJ*, 456, 766
- Skrutskie M. F. et al., 2006, *AJ*, 131, 1163
- Smith R. K., Brickhouse N. S., Liedahl D. A., Raymond J. C., 2001, *ApJ*, 556, L91
- Southworth J., 2010, *MNRAS*, 408, 1689
- Stelzer B., Damasso M., Scholz A., Matt S. P., 2016, *MNRAS*, 463, 1844
- Szabó G. M., Kiss L. L., 2011, *ApJ*, 727, L44
- Torres G., 2007, *ApJ*, 671, L65
- Triaud A. H. M. J. et al., 2013, *A&A*, 551, A80
- Triaud A. H. M. J. et al., 2015, *MNRAS*, 450, 2279
- Turner J. D., et al., 2017, *MNRAS*, 472:3871
- Turner J. D. et al., 2016, *MNRAS*, 459, 789
- Unruh Y. C., Solanki S. K., Fligge M., 1999, *A&A*, 345, 635
- Van Grootel V. et al., 2014, *ApJ*, 786, 2
- van Leeuwen F., 2007, *A&A*, 474, 653
- van Saders J. L., Ceillier T., Metcalfe T. S., Silva Aguirre V., Pinsonneault M. H., García R. A., Mathur S., Davies G. R., 2016, *Nature*, 529, 181
- Vidal-Madjar A., Lecavelier des Etangs A., Désert J.-M., Ballester G. E., Ferlet R., Hébrard G., Mayor M., 2003, *Nature*, 422, 143
- Vidal-Madjar A. et al., 2004, *ApJ*, 604, L69
- Walsh B. M., Kuntz K. D., Collier M. R., Sibeck D. G., Snowden S. L., Thomas N. E., 2014, *Space Weather*, 12, 387
- Watson A. J., Donahue T. M., Walker J. C. G., 1981, *Icarus*, 48, 150
- Wheatley P. J., Louden T., Bourrier V., Ehrenreich D., Gillon M., 2017, *MNRAS*, 465, L74
- Williams D. M., 2003, *Am. J. Phys.*, 71, 1198
- Wilms J., Allen A., McCray R., 2000, *ApJ*, 542, 914
- Wood B. E., Brown A., Linsky J. L., Kellett B. J., Bromage G. E., Hodgkin S. T., Pye J. P., 1994, *ApJS*, 93, 287
- Woods T. N. et al., 2005, *J. Geophys. Res. (Space Phys.)*, 110, A01312
- Wright N. J., Drake J. J., 2016, *Nature*, 535, 526
- Wright N. J., Drake J. J., Mamajek E. E., Henry G. W., 2011, *ApJ*, 743, 48 (W11)
- Youngblood A. et al., 2016, *ApJ*, 824, 101

## APPENDIX A: HIGH-PRECISION FAST PHOTOMETRY WITH THE XMM-NEWTON OM

In assessing the OM data for WASP-80, we noticed the outputs from the standard SAS analysis chains for the image and fast mode data, OMICHAIN and OMFCHAIN, respectively, did not fully agree with each other. Fig. A1 highlights the differences between the shape of the image mode light curve (red circles) and fast mode light curves (green squares and pink triangles; where the green squares are from the per-exposure source lists accompanying the fast mode light curve, and the pink triangles represent the fast mode time

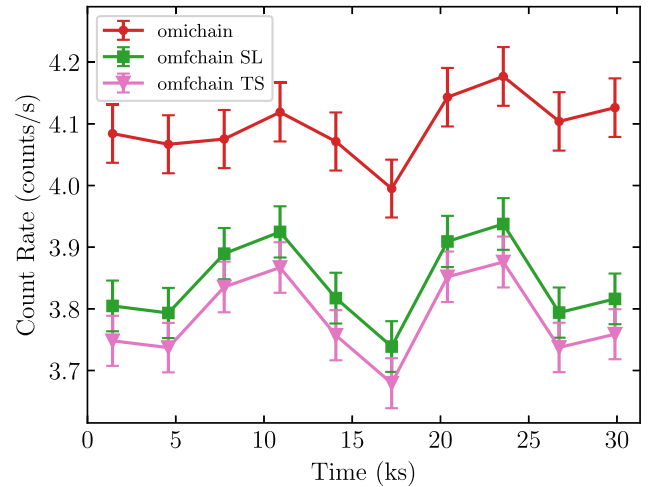


**Figure A1.** Comparison of the *XMM-Newton* OM light curves for WASP-80. The image mode data reduced by OMICHAIN are shown by the red circles. Two fast mode light curves from the OMFCHAIN outputs are displayed: one taken from the source list (SL) for each overall exposure (green squares), the other from the time series (TS) binned to the same cadence (pink triangles).

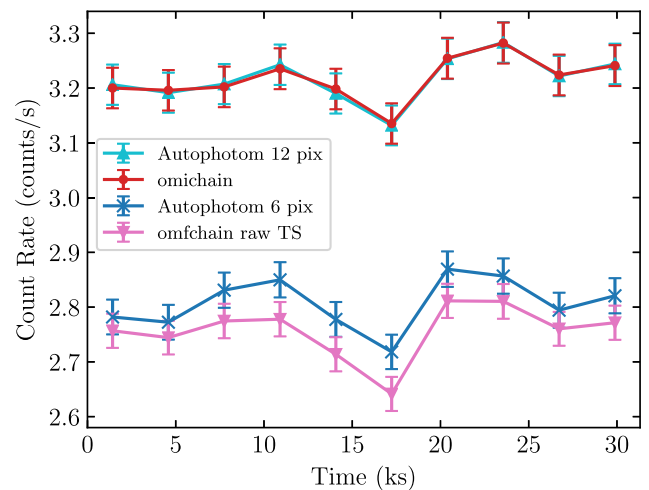


**Figure A2.** Comparison of the raw OMICHAIN (red circles) and OMFCHAIN time series (pink down-pointing triangles) with AUTOPHOTOM analyses using 12 (cyan up-pointing triangles) and 6 (blue crosses) pixel radii apertures. This shows the main difference between OMICHAIN and OMFCHAIN light curves is due to the different extraction radii used.

series binned to the same cadence, both from OMFCHAIN). The most obvious differences are the jump after the first two points and drop down before the last two points.

Our hypothesis for the cause of the discrepancy between the image and fast mode chains was that this was due to the different source apertures employed. OMICHAIN uses 12 pixel radii apertures for the image mode data, but OMFCHAIN uses only 6 pixel radii regions because of the small size of the fast mode window. Unfortunately, we could not test this hypothesis using the analysis chains. The aperture size used by OMICHAIN is not able to be modified, and although the sizes employed by OMFCHAIN are customizable, the fast mode window is far too small for apertures with a radius of 12 pixels to be used. Therefore, to test our hypothesis, we instead analysed the data using a standard photometry code.

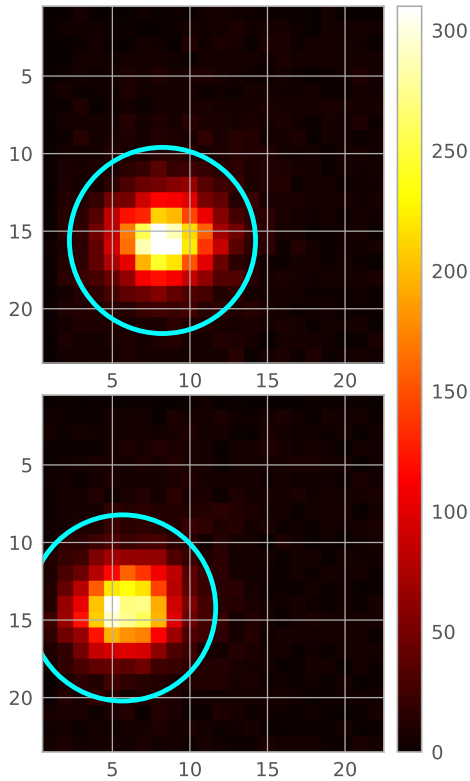


**Figure A3.** Comparison of two fast mode exposures, and how the source position within the window changes. For exposure 401 (top panel), the omfchain aperture used to extract the time series, overplotted in cyan, remains fully within the window. However, the aperture runs into the side of the window in exposure 007 (bottom panel), causing a small discrepancy with the corresponding image mode data when a same-sized aperture is used.

We performed aperture photometry on the image mode data using the AUTOPHOTOM routine, part of the PHOTOM package (Eaton, Draper & Allan 2009) from the STARLINK project (Currie et al. 2014). This

was done using source aperture radii of 12 and 6 pixels. These light curves, along with the raw light curves from the OMICHAIN and OMFCHAIN, are displayed in Fig. A2. Our 12 pixel aperture extraction using AUTOPHOTOM (shown as cyan up-pointing triangles) is in excellent agreement with the OMICHAIN light curve (red circles), and our 6 pixel aperture AUTOPHOTOM extraction is very similar in shape to the raw OMFCHAIN time series. This confirms our hypothesis that the main difference between OMICHAIN and OMFCHAIN can be attributed to the different extraction radii. However, there is slight difference in shape towards the middle of the observation, which points to a second effect (there is also an offset similar to that seen between the two OMFCHAIN outputs in Fig. A1).

We believe this second effect is the result of the source moving in the fast mode window, causing the extraction aperture to extend a little beyond the fast mode window for these exposures. This is highlighted in Fig. A3, which shows two fast mode window exposures: ‘401’ and ‘007’. The former is unaffected by this issue, whereas the latter is the worst afflicted. The points with a greater offset in the fast mode comparison in Fig. A2 correspond to the exposures where the PSF runs into the edge of the fast mode window.

We conclude that the differences in shape we see in Fig. A1 can be understood as primarily resulting from the different aperture sizes used, with a further, smaller contribution from the source aperture running into the sides of the fast mode window. Therefore, we feel justified in correcting fast mode data from OMFCHAIN by the corresponding image mode data from OMICHAIN. Taking the ratio of the image mode data to the fast mode time series binned to the same cadence (i.e. the ratio of the red and pink light curves in Fig. A1) provides a suitable correction. Each individual time bin in our analysis in Section 5.2 was therefore multiplied by this ratio, as calculated for the corresponding exposure.

This paper has been typeset from a  $\text{\TeX}/\text{\LaTeX}$  file prepared by the author.